IMAGE: A MAP OF THE STARS OF THE ORION CONSTELLATION

Print ISSN: 2631-8474 Online ISSN: 2631-8482

JournalPreview

London Journal of Engineering Research

Volume 21 | Issue 1 | Compilation 1.0

London Journals Press

JournalPreview

LONDON JOURNAL ENGINEERING RESEARCH

Journal Content
In this Issue

London Journals Press

Oxalate Salts: Synthesis and X-Ray Crystal Molecular Characterization of a 2-Methylimidazolium Containing H-Bonded $[C_2O_4HO_4C_2]^{3-}$ and a 2:1 DABCOH/urea Co-Crystal

Mouhamadou Birame Diop, Sérigne Cissé, Modou Sarr, Libasse Diop & David K. Geiger

Université Cheikh Anta Diop

ABSTRACT

Two new oxalate salts 0.5 $\{[(C_4H_7N_2)_3]\ [C_2O_4\ HC_2\ O_4]\}$(1) and $[(C_6H_{13}N_2)_2]\ [CH_4ON_2]\ [C_2O_4]$(2) have been isolated and characterized by single - crystal X-ray diffraction. Salt 1 crystallizes in the triclinic system, space group P-1 with a = 7.909 (14), b = 8.538 (14), c = 9.030(15) Å, α = 115.26 (4)°, β = 109.22 (7)°, γ = 95.38 (8)°, V = 500.7 (15) Å^3 and Z = 2. Salt 2 crystallizes in the monoclinic system, space group C2/c with a = 21.376 (4), b = 9.9127 (15), c = 19.046 (3) Å,β = 112.756 (9)°, V = 3721.6 (11)Å ^{3} and Z = 8. In 1, a hydrogen atom shared by two O atoms, from the hydrogen oxalate and oxalate, has a statistical occupancy of 0.5 on each O site leading to a 1:1 hydrogen oxalate/oxalate mixture in the crystal. One 2-methylimidazolium cation exhibits positional disorder. Hydrogen oxalate/oxalate pairs are linked by cations via N–H···(O,O) hydrogen bonds leading to chains, which are then connected through N–H···O hydrogen bonds yielding a sheet structure. C–H···O hydrogen bonds are also present in the crystal. In the co-crystal 2, the monoprotonated DABCO and urea molecules are connected to the oxalate through N–H···(O,O) bifurcated hydrogen bonds and N–H···O hydrogen bonds, respectively. Moreover, N–H···N hydrogen bonds link monoprotonated DABCO to urea molecules in addition to inner C–H···$O_{oxalate}$ interactions and intermolecular C–H···O_{urea} hydrogen bonding interactions. The interspecies hydrogen bonding interactions give rise to a supramolecular three-dimensional structure. In both compounds 1 and 2, the oxalate anion is twisted.

Keywords: crystal, hydrogen oxalate/oxalate 1:1 mixture, DABCOH/urea 2:1 co-crystal, hydrogen bonds, 2-methyl imidazolium, DABCO, sheet, 3D structure.

Classification: FOR Code: 039999

Language: English

London Journals Press

LJP Copyright ID: 392961
Print ISSN: 2631-8474
Online ISSN: 2631-8482

London Journal of Engineering Research

Volume 21 | Issue 1 | Compilation 1.0

Oxalate Salts: Synthesis and X-Ray Crystal Molecular Characterization of a 2-Methylimidazolium Containing H-Bonded $[C_2O_4HO_4C_2]^{3-}$ and a 2:1 DABCOH/urea Co-Crystal

Mouhamadou Birame Diop[α], Sérigne Cissé[σ], Modou Sarr[ρ], Libasse Diop[ω] & David K. Geiger[¥]

ABSTRACT

Two new oxalate salts 0.5 {[$(C_4H_7N_2)_3$] [$C_2O_4HC_2O_4$]}(1) and [$(C_6H_{13}N_2)_2$] [CH_4ON_2] [C_2O_4](2) have been isolated and characterized by single - crystal X-ray diffraction. Salt 1 crystallizes in the triclinic system, space group P-1 with a = 7.909 (14), b = 8.538 (14), c = 9.030(15) Å, α = 115.26 (4)°, β = 109.22 (7)°, γ = 95.38 (8)°, V = 500.7 (15) Å^3 and Z = 2. Salt 2 crystallizes in the monoclinic system, space group C2/c with a = 21.376 (4), b = 9.9127 (15), c = 19.046 (3) Å, β = 112.756 (9)°, V = 3721.6 (11) Å^3 and Z = 8. In 1, a hydrogen atom shared by two O atoms, from the hydrogen oxalate and oxalate, has a statistical occupancy of 0.5 on each O site leading to a 1:1 hydrogen oxalate/oxalate mixture in the crystal. One 2-methylimidazolium cation exhibits positional disorder. Hydrogen oxalate/oxalate pairs are linked by cations via N–H···(O,O) hydrogen bonds leading to chains, which are then connected through N–H···O hydrogen bonds yielding a sheet structure. C–H···O hydrogen bonds are also present in the crystal. In the co-crystal 2, the monoprotonated DABCO and urea molecules are connected to the oxalate through N–H···(O,O) bifurcated hydrogen bonds and N–H···O hydrogen bonds, respectively. Moreover, N–H···N hydrogen bonds link monoprotonated DABCO to urea molecules in addition to inner C–H···$O_{oxalate}$ interactions and intermolecular C–H···O_{urea} hydrogen bonding interactions. The interspecies hydrogen bonding interactions give rise to a supramolecular three-dimensional structure. In both compounds 1 and 2, the oxalate anion is twisted.

Keywords: crystal, hydrogen oxalate/oxalate 1:1 mixture, DABCOH/urea 2:1 co-crystal, hydrogen bonds, 2-methyl imidazolium, DABCO, sheet, 3D structure.

Author α σ ρ ω: Laboratoire de Chimie Minérale et Analytique (LA.CHI.MI.A), Département de Chimie, Faculté des Sciences et Techniques, Université Cheikh Anta Diop, Dakar, Senegal.

¥: Department of Chemistry, SUNY-College at Geneseo, GENESEO, NY 14454, USA.

I. INTRODUCTION

In crystal engineering, protonated amines play a pivotal role because of the supramolecular structures they display. Many groups of researchers are focusing on synthesizing such types of materials which have shown interesting physical properties [1-3]. In these amine salts hydrated or not, the amine can be neutral or protonated, the anionic component being acidic or non-acidic: they are soluble in organic solvents and are used in the study of their interactions with metallic halides, acetates and organotins for example, to isolate new complexes. In the field of DABCO-based ionic liquids, a DABCO inorganic-organic hybrid salt has recently been prepared and used to catalyze syntheses of pyrimido [4, 5-b] -quinoline and pyrimido [4, 5-d] pyrimidine derivatives [4]. Oxalate complexes with interesting properties such as fluorescence, proton conductivity, magnetic and quantum spin liquid are known [5-8]. Oxalate salts containing the hydrogen bonded anion $[C_2O_4HO_4C_2]^{3-}$ with bulky cations have been reported [9-12]. For decades, the Dakar group has focussed on the

London Journal of Engineering Research

synthesis and characterization of oxalate organo and halotin complexes [13-19]. Vaidhyanathan and coworkers have reported the crystal structures of some protonated amine salts among which DABC- $OH_2(HC_2O_4)_2$ [20] which consists of hydrogen bonded dimers of $[HC_2O_4]^-$ linked to $DABCOH_2$ dications through N-H···O hydrogen bonds. This salt is the reaction product between DABCO diamine and oxalic acid in water at 85°C. As continuation of this research program, we initiated in this work the study of the interactions between 2-methyl imidazole and oxalic acid in the presence of trimethyltin chloride ($SnMe_3Cl$) and, took back in situ, changing the solvent and the thermal conditions, the Vaidhyanathan and co-workers reaction [20] and ground into a solution of urea: this yielded single crystals of the 2-methylimidazolium oxalate/H/oxalate (1) and the DABCOH/urea co-crystal (2) whose X-ray analyses have been carried out and reported herein.

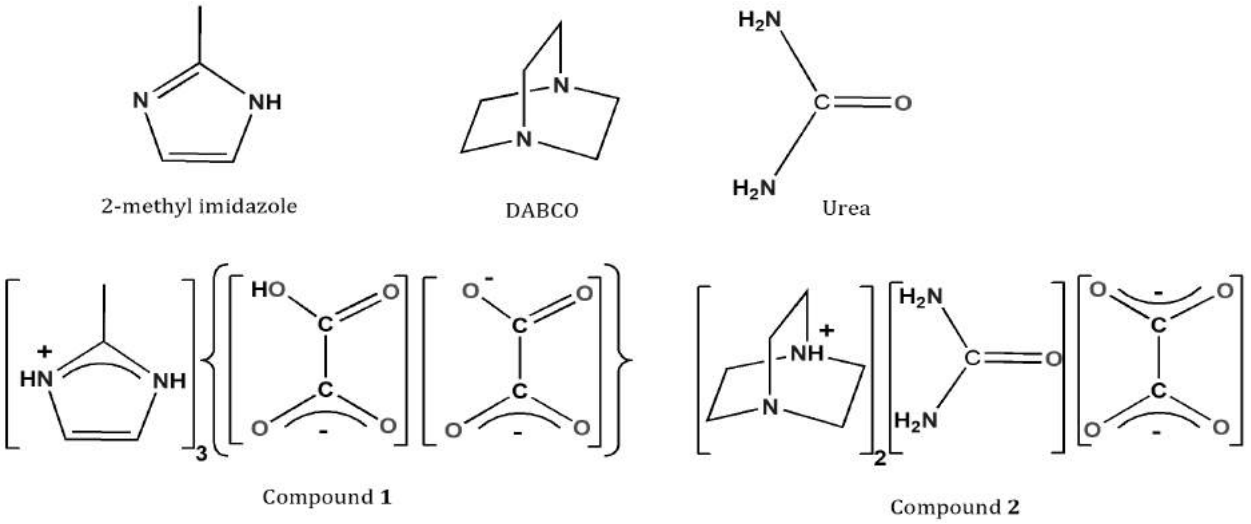

Scheme 1: Molecular representations of 2-methyl imidazole, DABCO and urea reagents, and compounds (**1** and **2**) related to this work

II. Materials and methods

2.1 General

Chemicals were purchased from Sigma-Aldrich (Germany) and were used without any further purification. Infrared spectrum was recorded on a Bruker Vector 22 spectrometer equipped with a Specac Golden Gate™ ATR device.

2.2 Synthesis and crystallization of 0.5[[$(C_4H_7N_2)_3$][$C_2O_4HC_2O_4$]] (1)

A 5 mL aqueous solution of 2-methyl imidazole, $C_4H_6N_2$ [0.704 mmol (57.8 mg)] added to a 10 mL aqueous solution of oxalic acid dihydrate, $H_2C_2O_4.2H_2O$ [0.704 mmol (88.8 mg)] gave a clear solution. After stirring 1h at room temperature in the open atmosphere, a 15 mL methanol solution of trimethyltin chloride, $SnMe_3Cl$ [0.352 mmol (70.1 mg)] was added dropwise. The clear solution was stirred 2 h at room temperature in the open atmosphere. Colorless prism-like crystals suitable for a single-crystal X-ray diffraction analysis were obtained after some days of slow solvent evaporation at room temperature and finally characterized as **1**.

2.3 Synthesis and crystallization of [$(C_6H_{13}N_2)_2$][CH_4ON_2][C_2O_4] (2)

By reacting 6 mL ethanol solution of DABCO, $C_6H_{12}N_2$ [0.506 mmol (56.8 mg)] and 15 mL ethanol solution of oxalic acid dihydrate, $H_2C_2O_4.2H_2O$ [1.012 mmol (127.6 mg)], a clear solution is obtained then stirred 1h at room temperature. Adding dropwise a 15 mL ethanol solution of urea, CH_4N_2O [0.506 mmol (30.4 mg)] at room temperature, the solution remains clear then stirred 2h in the open atmosphere. After some days of a slow solvent evaporation at room temperature, colorless block-like crystals suitable for a single-crystal X-ray diffraction analysis were afforded and finally characterized as **2**.

III. X-RAY CRYSTALLOGRAPHY

Crystals of approximate dimensions 0.650× 0.300×0.200 mm for **1** and 0.400×0.350×0.350 mm for **2** were used for data collection. The X-ray crystallographic data for salts **1** and **2** were collected using a Bruker SMART X2S benchtop diffractometer operating at *T*=200 (2) K. Data for 1 and 2 were measured using φ and ω scans of 0.5° using Mo*K*α radiation (λ = 0.71073 Å) using a collection strategy to obtain a hemisphere of unique data determined by Apex2 [21] and Apex3 [22], respectively. Cell parameters were retrieved and refined using the SAINT software (Version 8.34A-2013) [23]. Data reduction was performed using the SAINT software which corrects for Lorentz polarization [23]. The structures were solved by the Direct Methods using the ShelXS [24] structure solution program and refined by Least Squares using ShelXL [25].

Programs used for the representation of the molecular and crystal structures: Platon [26] and Mercury [27]. The Crystallographic data and experimental details for structural analyses of **1** and **2** are summarized in Table 1. Selected geometric parameters for compounds **1** and **2** are listed in Tables 2 and 3, respectively.

CCDC 1857217 (**1**) and 1951785 (**2**) contain the supplementary crystallographic data for this paper. These data can be obtained free of charge via https://www.ccdc.cam.ac.uk/structures/, or by e-mailing data_request@ccdc.cam.ac.uk, or by contacting The Cambridge Crystallographic Data Centre, 12 Union Road, Cambridge CB2 1EZ, UK; fax: +44(0)1223-336033.

Table 1: Crystal data and structure refinement for compounds **1** and **2**

Parameters	Compound 1	Compound 2
Empirical formula	$C_8H_{11}N_3O_4$	$C_{15}H_{30}N_6O_5$
Formula weight	213.20	374.45
Temperature	200 (2) K	200 (2) K
Wavelength	0.71073 Å	0.71073 Å
Crystal system	Triclinic	Monoclinic
Space group	*P-1*	*C2/c*
Unit cell dimensions	a = 7.909(14) Å α = 115.26 (4)° b = 8.538(14) Å β = 109.22 (7)° c = 9.030(15) Å γ = 95.38 (8)°	a = 21.376 (4) Å α = 90° b = 9.9127 (15) Å β = 112.756 (9)° c = 19.046 (3) Å γ = 90°
Volume	500.7 (15) Å^3	3721.6 (11) Å^3
Z	2	8
Calculated density	1.414 g cm^{-3}	1.337 g cm^{-3}
Absorption coefficient	0.115 mm^{-1}	0.101 mm^{-1}
F(000)	224	1616
Crystal size	0.650 × 0.300 × 0.200 mm^3	0.400 × 0.350 × 0.350 mm^3
Theta range for data collection	2.735–27.869°	2.2952–24.8645°
Limiting indices	-10≤ *h* ≤10, -10≤ *k* ≤ 11, -11≤ *l* ≤11	-27≤ *h* ≤17, -12≤ *k* ≤ 12, -20≤ *l* ≤24
Reflections collected/unique	9133/2319	16793/4081
R_{int}	0.1012	0.0961
Absorption correction	Multi-scan	Multi-scan
Max. and min. transmission	0.977 and 0.929	0.96 and 0.65
Refinement method	Full-matrix least-squares on F^2	Full-matrix least-squares on F^2
Data/restraints/parameters	2319/154/186	4081/0/260
Goodness-of-fit on F^2	1.077	1.030
Final R indices ($I > 2\sigma(I)$)	R_1 = 0.0681, wR_2 = 0.2121	R_1 = 0.0651, wR_2 = 0.2040
R indices (all data)	R_1 = 0.0823, wR_2 =0.1941	R_1 = 0.0952, wR_2 =0.1794
Largest diff. peak and hole	0.581 and -0.248 e Å^{-3}	0.304 and -0.352 e Å^{-3}

$w = 1/[\sigma^2(F_o^2) + (0.1076P)^2 + 0.1053P]$ for **1**, $w = 1/[\sigma^2(F_o^2) + (0.1248P)^2]$ for **2**, where $P = (F_o^2 + 2F_c^2)/3$

Table 2: Selected bond lengths (Å) and angles (°) for compound **1**

Atom—Atom	Bond length	Atom—Atom	Bond length
O1—C9	1.253 (3)	C2—C3	1.341 (4)
O2—C9	1.240 (3)	C3—N2	1.369 (3)
O3—C10	1.217 (3)	C5—N3	1.333 (7)
O4—C10	1.272 (3)	C5—N4	1.338 (8)
C9—C10	1.563 (3)	C5—C8	1.422 (8)
C1—N2	1.317 (3)	N3—C6	1.374 (8)
C1—N1	1.333 (4)	C6—C7	1.331 (8)
C1—C4	1.478 (3)	C7—N4	1.378 (10)
N1—C2	1.367 (3)		
Atom-atom-atom	Angle value	Atom-atom-atom	Angle value
O2—C9—O1	125.00 (16)	C3—C2—N1	106.9 (2)
O2—C9—C10	117.7 (2)	C2—C3—N2	107.2 (3)
O1—C9—C10	117.25 (18)	C1—N2—C3	109.0 (2)
O3—C10—O4	125.76 (16)	N3—C5—N4	105.5 (5)
O3—C10—C9	118.8 (2)	N3—C5—C8	128.9 (6)
O4—C10—C9	115.28 (18)	N4—C5—C8	125.6 (6)
N2—C1—N1	108.1 (2)	C5—N3—C6	110.5 (5)
N2—C1—C4	125.9 (2)	C7—C6—N3	106.9 (6)
N1—C1—C4	126.0 (2)	C6—C7—N4	106.7 (6)
C1—N1—C2	108.8 (2)	C5—N4—C7	110.3 (5)
O1—C9—C10—O3	-27.1 (3)	O2—C9—C10—O4	-26.3 (3)

Table 3: Selected bond lengths (Å) and angles (°) for compound **2**

Atom—Atom	Bond length	Atom—Atom	Bond length
O1—C13	1.250 (2)	N3—C11	1.471 (3)
O2—C13	1.243 (2)	N4—C10	1.484 (3)
O3—C14	1.255 (2)	N4—C12	1.488 (3)
O4—C14	1.257 (2)	N4—C8	1.490 (3)
O5—C15	1.224 (3)	N5—C15	1.353 (3)
N1—C6	1.481 (3)	N6—C15	1.347 (3)
N1—C3	1.485 (3)	C1—C2	1.538 (3)
N1—C1	1.491 (3)	C3—C4	1.540 (3)
N2—C5	1.454 (3)	C5—C6	1.527 (3)
N2—C2	1.455 (3)	C7—C8	1.542 (3)
N2—C4	1.462 (3)	C9—C10	1.540 (3)
N3—C9	1.458 (3)	C11—C12	1.532 (3)
N3—C7	1.462 (3)	C13—C14	1.536 (3)
Atom-atom-atom	Angle value	Atom-atom-atom	Angle value
C6—N1—C3	109.62 (19)	C7—N3—C11	107.71 (18)
C6—N1—C1	109.05 (17)	C10—N4—C12	110.73 (19)
C3—N1—C1	110.77 (19)	C10—N4—C8	109.78 (16)
C5—N2—C2	108.3 (2)	C12—N4—C8	109.03 (18)
C5—N2—C4	107.5 (2)	O5—C15—N6	122.34 (19)
C2—N2—C4	109.9 (2)	O5—C15—N5	122.5 (2)
C9—N3—C7	108.94 (19)	N6—C15—N5	115.1 (2)
C9—N3—C11	109.4 (2)		
O2—C13—C14—O3	-18.3 (3)	O1—C13—C14—O4	-18.3 (3)

IV. RESULTS

Compound **1** was isolated from reaction between an aqueous solution and a methanol solution.

Oxalic acid dihydrate, ($H_2C_2O_4.2H_2O$) and 2-methylimidazole, ($C_4H_6N_2$) were preliminarily mixed at room temperature, giving a clear solution. To this clear aqueous solution was added dropwise an equimolar methanol solution of trimethyltin chloride, $SnMe_3Cl$. Colorless single cr stals rew E . 1 from the lim id solution and

were characterized as 1, 0.5{[$(C_4H_7N_2)_3$][$C_2O_4HC_2O_4$]}.

Similarly, salt 2 was isolated from reaction in ethanol between oxalic acid dihydrate ($H_2C_2O_4.2H_2O$), 1,4-diazabicyclo [2.2.2] octane (DABCO) and urea, CH_4ON_2. Ethanol solutions of oxalic acid dihydrate ($H_2C_2O_4.2H_2O$) and DABCO were first mixed in a 2:1 ratio. An ethanol solution of urea was then added to the mixture at room temperature leading to the formation of [$(C_6H_{13}N_2)_2$] [CH_4ON_2] [C_2O_4] (2) collected as colorless crystals (Eq. 2). In 2002, Vaidhyanathan and coworkers have isolated $DABCOH_2(HC_2O_4)_2$ [20] using the same reaction, in water, between DABCO and oxalic acid in 1:2 ratio at 85°C. The aim of the addition of urea was to have two varieties of cations by neutralizing the hydrogen oxalate that may be afforded after protonation of the DABCO diamine. Recently, we have isolated and characterized an inorganic-organic hybrid complex with mixed cations [28]. To date, numerous DABCOH organic or inorganic-organic hybrid salts have been isolated and structurally characterized [29-32]. This is the first co-crystal example including both DABCOH and urea. The yields of the reactions reported herein are 47% and 35%, respectively.

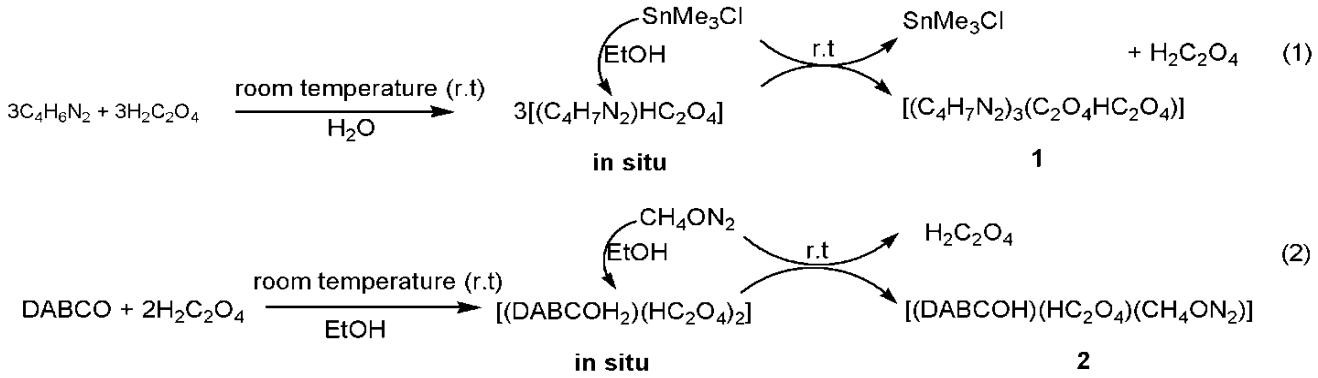

V. DISCUSSION

*5.1 Crystal and molecular structure of salt 0.5[[$(C_4H_7N_2)_3$][$C_2O_4HC_2O_4$]] (**1**)*

5.1.1 FT-IR spectroscopy

Crystals of **1** were investigated by FT-IR spectroscopy in ATR mode. FT-IR spectrum evidence absorption bands that can be assigned to 2-methylimidazolium cation (N–H, N–C, C–H, C=C and C=N bonds) and oxalate anion. In the literature, several works with FT-IR imidazolium vibration bands investigation have previously been reported [33-42] as well as carboxylates especially oxalate [20, 43, 44]. Thus, the band due to C=C stretching vibrations is overlapped by $\upsilon as CO_2$. The bands located at 1514 cm^{-1} and 1438 cm^{-1} are attributed to N–H and C–H bending vibrations, whereas those at 1242 cm^{-1} may correspond to υsCO_2 or C–N stretching vibrations of the imidazolium. The C–N deformation vibrations and the rocking CH_3 vibrations present about 1000-1100 cm^{-1} are partially overlapped by some imidazolium ring vibrations. The bands observed at 765 cm^{-1} and 753 cm^{-1} are assigned to the imidazolium out of plane ring vibrations. The presence of the 2-methylimidazolium cation is also confirmed by the absorptions observed at 3188 cm^{-1} and 3151 cm^{-1}, assigned to N–H stretching vibrations while the absorption at 2923 cm^{-1} is attributed to C–H stretching vibrations in the imidazolium ring. Moreover, the band located at 3512 cm^{-1}, attributed to υOH, evidences the presence of the hydrogen oxalate.

5.1.2 Molecular characterization

Salt (**1**) crystallizes in the centrosymmetric triclinic P-1 space group about the inversion centre at [0, 0.5, 0], thus, only half of the molecule is observed in the asymmetric unit. The hydrogen atom H4O attached to O4 of the hydrogen oxalate has a statistical occupancy of 0.5, thus leading to a 1:1 mixture of a hydrogen oxalate and an oxalate in the crystal applying symmetry operation (i) -*x*, 1-*y*, -*z* (Fig. 1).

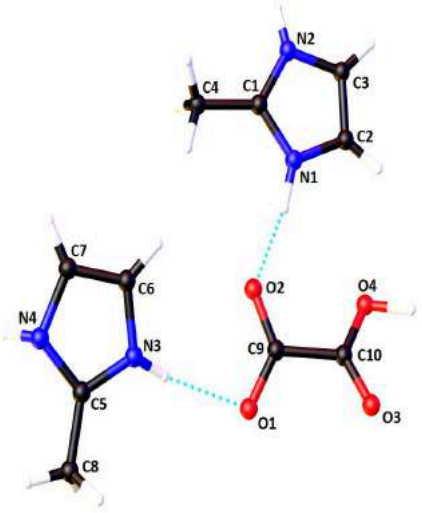

Figure 1: View of **1** showing the atom-labeling scheme. Only one orientation of the disordered fragments is represented. Anisotropic displacement parameters of non-hydrogen atoms are represented at the 50% probability level. [atom color code: C, gray; H, white; N, blue; O, red]

We earlier have reported a structure containing a hydrogen atom with 0.5 occupancy in a 1:1 mixture of a 2-methylimidazole molecule and a 2-methyl-1*H*-imidazol-3-ium cation [45]. A 2-methyl-1*H*-imidazol-3-ium cation was found to be positional disordered by approximately 180° rotation perpendicular to the plane of the imidazolium ring. The geometric parameters within the imidazolium rings are consistent with π delocalization and are in the reported range [45-48]. The CO distances observed about C(10) (Table 2) are in accordance with double C = O and single C – O bonds for oxalate anion, respectively [17-19, 45, 47]. The CO bonds about C(9),on the contrary, are consistent with a delocalization [18, 45, 49], the longer resulting from its involvement in two hydrogen bonds with two distinct cations. The torsion angles within the oxalate indicate unexpectedly that this last is twisted as previously found in the literature [19, 50]. Pairs of hydrogen oxalate/oxalate are connected through cations *via* bifurcated N–H···(O,O) hydrogen bonds, giving rise to chains (Fig. 2 and Table 4).

Figure 2: Partial packing diagram of **1** showing the chains along [011] formed by N–H...O hydrogen bonds. Only hydrogen atoms involved in the interactions are shown. Symmetry identifiers are those found in Table 2. Only one orientation of the disordered fragments is shown

These chains are then connected into a sheet approximately parallel to the (2 1 -1) plane through N–H···O hydrogen bonding interactions involving O1 and the disordered cation (Fig. 3 and Table 4). In the chains, the 2-methyl imidazolium cations as well as the hydrogen oxalate/oxalate pairs, are oriented in an isotactic manner. The H···O hydrogen bond length observed in the

anionic pair of 1.47 (6) Å is less than the reported values of 1.73 (3) Å [9] and 1.59 Å [10] but greater than the reported values of 1.24 Å [11] and 1.232 (3) Å [12]. The smaller values of 1.24 Å and 1.232 (3) Å are presumably due to the H atom which is located midway between the two O oxalate atoms edge-sharing it. Additional C–H···O hydrogen bonds strengthen the layer resulting from the interspecies hydrogen bonding interactions (Table 4). A comparison (O–H···O and H···O parameters) is given in Table 5.

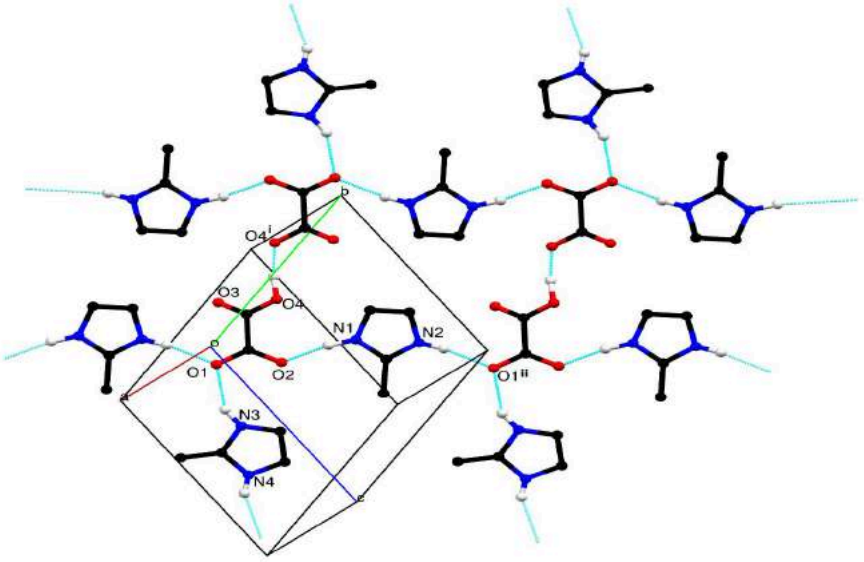

Figure 3: Partial packing diagram of **1** showing the hydrogen-bonded sheets parallel to (2 1-1). Only hydrogen atoms involved in the interactions are shown. Symmetry identifiers are those found in Table 4. Only one orientation of the disordered fragments is shown.

Table 4: Hydrogen-bond geometry (Å, º) for compound **1** (Symmetry codes: (i) $-x, -y+1, -z$; (ii) $x, y+1, z+1$; (iii) $-x, -y+1, -z+1$; (iv) $-x+1, -y, -z+1$; (v) $x, y-1, z$)

D–H···*A*	*D*–H	H···*A*	*D*···*A*	*D*–H···*A*
O4–H4O···O4^{i}	1.06 (7)	1.47 (6)	2.490 (4)	158 (5)
N1–H1N···O2	0.97 (3)	1.76 (3)	2.715 (4)	170 (2)
N1–H1N···O4	0.97 (3)	2.64 (3)	3.198 (6)	117 (2)
C2–H2···O3^{i}	0.95	2.41	3.333 (6)	162.7
C3–H3···O3^{ii}	0.95	2.48	3.018 (5)	115.6
N2–H2N···O1^{ii}	0.89 (3)	1.88 (3)	2.762 (5)	170 (3)
N2–H2N···O3^{ii}	0.89 (3)	2.64 (3)	3.105 (6)	114 (3)
C4–H4C···O4^{iii}	0.98	2.57	3.464 (6)	151.3
N3–H3N···O1	0.88 (2)	2.03 (5)	2.811 (7)	148 (7)
C6–H6···O2	0.95	2.50	3.032 (7)	115.4
N4–H4N···O1^{iv}	0.88 (2)	1.99 (5)	2.767 (7)	147 (7)
C8–H8B···O4^{v}	0.98	2.68	3.649 (12)	169.1

Based on the formula, $C_6H_{11}N_3O_4$, the salt (**1**) can be seen as an adduct of di-2-methyl imidazolium oxalate, $C_{10}H_{14}N_4O_4$, reported by Callear and coworkers [48], and of dehydrated 2-methyl imidazolium hydrogen oxalate dihydrate we earlier reported [45]. In conclusion, full molecular salt (**1**), $C_{16}H_{22}N_6O_8$ = di-2-methyl imidazolium oxalate ($C_{10}H_{14}N_4O_4$) [48] + 2-methyl imidazolium hydrogen oxalate ($C_6H_8N_2O_4$). Within the isolation of salt **1**, the trimethyl tin(IV), $SnMe_3Cl$ presumably acts as a catalyst.

5.2 Crystal and molecular structure of salt [$(C_6H_{13}N_2)_2$][CH_4ON_2][C_2O_4] (2)

The 2:1 DABCOH/urea co-crystal **2** crystallizes in the monoclinic C2/*c* space group. Its asymmetric unit depicted in Fig. 4 comprises two monoprotonated DABCO (DABCOH), one oxalate, and one urea molecule. The DABCOH are linked to the oxalate through N–H···(O,O) bifurcated hydrogen bonds while the urea molecule binds the oxalate *via* two N–H···O hydrogen bonds (Table 6), leading to a discrete four components molecule. Each molecule is connected to two neighbours through N–H···N hydrogen bonding interactions involving hydrogen atoms of the urea molecule and two nitrogen atoms from two DABCOH (Table 6). In addition to the inner C–H···$O_{oxalate}$ interactions, intermolecular C–H··· O_{urea} hydrogen bonds connect the neighbouring molecules giving rise to a supramolecular three-dimensional structure (Fig. 5 and Table 6). In **2**, the CO lengths observed about the oxalate, slightly different due to their involvement in hydrogen bonding interactions, are comparable to those in compound **1** and are consistent with a π delocalization [18, 45, 49]. Comparing the geometric parameters with those of **1**, the torsion angles within **2** also indicate a twisted oxalate [19, 50]. The geometric parameters within the DABCOH and the urea molecule (Table 3) are comparable to previously reported values for DABCOH diamine and urea containing materials [51-54]. Moreover, all DABCOH cations are oriented so that they are almost parallel, whereas oxalate anions and urea molecules are disposed in two manners.

The neutral [$(DABCOH)_2$][C_2O_4] salt has never been reported, only its monoacidic homologue has been. The oxalate entanglement in **1** is nevertheless more emphasized than in **2**.

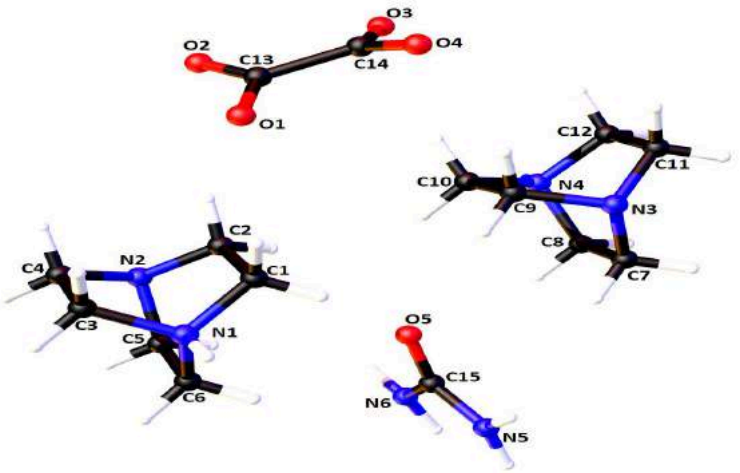

Figure 4: ORTEP view of the molecular structure of **2** showing the atom-labeling scheme. Anisotropic displacement parameters of non-hydrogen atoms are represented at the 50% probability level

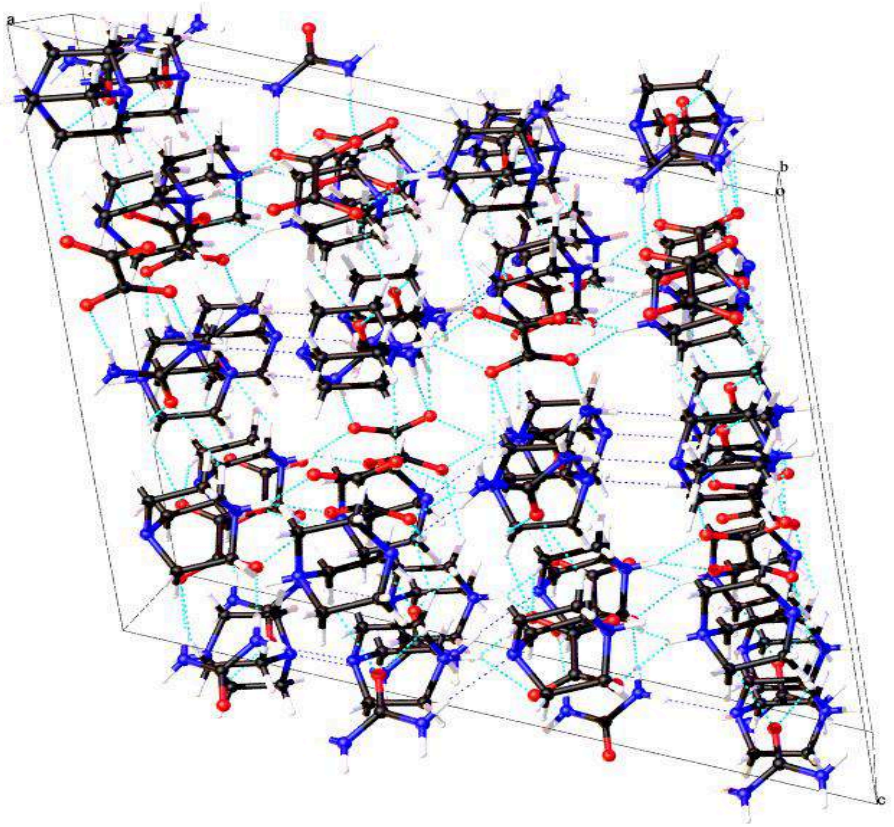

Figure 5: Crystal packing of the salt **2** showing the interlinked planes parallel to (100). Displacement ellipsoids are drawn at the 30% probability level. Symmetry identifiers are those found in Table 6

Table 6: Hydrogen-bond geometry (Å, º) for compound **2** (Symmetry codes: (i) -*x*+1, *y*, -*z*+1/2; (ii) -*x*+1/2, *y*+1/2, -*z*+1/2; (iii) *x*, -*y*+1, *z*-1/2; (iv) -*x*+1/2, -*y*+1/2, -*z*; (v) *x*, -*y*, *z*-1/2; (vi) *x*, *y*+1, *z*)

D–H···*A*	*D*–H	H···*A*	*D*···*A*	*D*–H···*A*
N1–H1···O1^{i}	0.96 (3)	1.97 (3)	2.736 (2)	136 (3)
N1–H1···O4^{i}	0.96 (3)	2.10 (3)	2.888 (2)	139 (2)
N4–H4···O2^{ii}	0.91 (2)	1.94 (3)	2.702 (2)	141 (2)
N4–H4···O3^{ii}	0.91 (2)	2.19 (3)	2.919 (2)	136 (2)
N5–H5*NA*···N3^{i}	0.86 (3)	2.33 (3)	3.179 (3)	169 (3)
N5–H5*NB*···O4^{iii}	1.00 (4)	1.99 (4)	2.988 (3)	173 (3)
N6–H6*NA*···N2^{iv}	0.89 (3)	2.23 (3)	3.116 (2)	170 (2)
N6–H6*NB*···O3^{iii}	1.00 (3)	1.97 (3)	2.969 (3)	176 (2)
C1–H1*A*···O5	0.99	2.45	3.240 (3)	137
C1–H1*B*···O1	0.99	2.51	3.370 (3)	145
C3–H3*B*···O4^{v}	0.99	2.56	3.477 (4)	155
C7–H7*B*···O1^{vi}	0.99	2.55	3.492 (3)	159
C10–H10*A*···O5	0.99	2.55	3.350 (3)	138

VI. CONCLUSION

The desired complex is not isolated in the presence of trimethyltin chloride ($SnMe_3Cl$). Salt **1** is layered formed by interspecies hydrogen bonds between 1:1 hydrogen oxalate/oxalate pairs and 2-methyl imidazolium cations. The structure of salt **1** is the seat of a disordered hydrogen atom located on two oxygen atom sites of two oxalates. The trimethyltin chloride, $SnMe_3Cl$, acts in the isolation of **1**, such a catalyst, promoting the transfer of the hydrogen atom. In salt **2**, the inter-species hydrogen bonding interactions lead to a supramolecular three-dimensional structure. As uncommon, the oxalate anions are twisted both in **1** and **2**. Continuing our investigations on isolation and characterization of 2-methyl

imidazolium and DABCOH oxalate organic and organometallic compounds, reactivity of **1** and **2** toward alkyl tin(IV), halotin(IV) and some MX_2 is in progress. To focus on the main function of trimethyltin chloride, $SnMe_3Cl$ within the isolation of salt **1**, reactions between 2-methyl imidazole, oxalic acid dihydrate and, $SnMe_3Cl$ in various proportions, some trialkyl tin(IV) such as triphenyltin (IV) and tributyltin (IV) are also being investigated in our laboratory.

ACKNOWLEDGEMENTS

The authors gratefully acknowledge the Cheikh Anta Diop University of Dakar (Senegal) and SUNY-College, Geneseo, NY (USA) for financial support.

REFERENCES

1. Li, C.-P., Nie, L., Pei, W.-B., Li, L., Tian, Z.-F., Liu, J.-L., Gao, X.-S., Ren, X.-M. (2016). Magnetic feature and near-infrared absorption of a $[Pt(mnt)_2]^-$-based H-bond supramolecular crystal. J. Solid State Chem. 243, 38-43.
2. Fu, J., Zheng, L., Yuan, Y., Song, Y., Xu, Y. (2011). Hydrothermal synthesis, crystal structure and properties of two organic amine templated lanthanide sulfates. J. Chem. Crystallogr. 41, 1737-1741.
3. Katrusiak, A. Szafranski, M. (1999). Ferroelectricity in NH···N Hydrogen Bonded Crystal. Phys. Rev. Lett. 82, 576-579.
4. Shirini, F., Langarudi, M. S. N., Daneshvar, N., Jamasbi, N., Irankhah-Khanghah, M. (2018). Preparation and characterization of [H_2-DABCO] $[ClO_4]_2$ as a new member of DABCO-based ionic liquids for the synthesis of pyrimido [4,5-b]-quinoline and pyrimido [4,5-d] pyrimidine derivatives. J. Mol. Struct. 1161, 366-382.
5. Yamada, T.,Sadakiyo, M., Kitagawa, H.(2009). High Proton Conductivity of One Dimensional Ferrous Oxalate Dihydrate. J. Am. Chem. Soc. 131, 3144-3145.
6. Zhang, B., Baker, P. J., Zhang, Y., Wang, D., Wang, Z., Su, S., Zhu, D., Pratt, F. L. (2018). Quantum Spin Liquid from a Three Dimensional Copper-Oxalate Framework. J. Am. Chem. Soc. 140, 122-125.
7. Clemente-Leon, M., Coronado, E., MartiGastaldo, C., Romero, F. M. (2011). Multifunctionality in hybrid magnetic materials based on bimetallic oxalate complexes. Chem. Soc. Rev. 40, 473-497.
8. Yamada, M. G., Fujita, H., Oshikawa, M. (2017). Designing Kitaev Spin Liquids in Meta l-Organic Frameworks. Phys. Rev. Lett. 119, 057202.
9. Delori, A., Galek, P. T. A., Pidcock, E., Jones, W. (2012). Quantifying Homo- and Heteromolecular Hydrogen Bonds as a Guide for Adduct Formatio. Chem. Eur. J. 18, 6835-6846.
10. Mouchaham, G., Gualino, M., Roques, N., Duhayon, C., Brandès, S., Sutter, J.-P. (2015). Supramolecular open-framework architecture based on dicarboxylate H-bond acceptors and polytopic cations with three/four N–H^+ donor units. CrystEngComm. 17, 8906-8914.
11. Nelson, J., Nieuwenhuyzen, M., Pál, I., Town, R. M. (2004). Steric complementarity in carboxylate anion recognition. Dalton Trans. (2004), 229-235.
12. Herbstein, F. H., Kapon, M. (1999). 8,11-Diaza[4.3.3]propell-6-enium Oxalate 2.5 hydrate. Z. Kristallogr. 214, 64-70.
13. Gueye, O., Qamar, H., Diop, L., Diop, C. A., Russo, U. (1993). A new synthetic route for mono and poly-tin (IV) oxalate adducts, IR and Mössbauer study. Polyhedron, 12, 1245-1249.
14. Diop, L., Mahieu, B., Mahon, M. F., Molloy, K. C., Okio, K. Y. A. (2003). Bis (triphenyltin) oxalate. Appl. Organomet. Chem. 17, 881-882.
15. Sow, Y., Diop, L., Kociock-Köhn, G., Molloy, K.C. (2010). X-ray crystal structure of $(nPr_2NH_2)_2C_2O_4.SnCl_4$. Main Group Met. Chem. 33, 205-208.
16. Sarr, M. Diasse-Sarr, A. Diallo, W., Plasseraud, L., Cattey, H. (2013). Bis (cyclohexyl ammo- nium) tetrachloride (oxalato) stannate (IV). Acta Crystallogr. E69, m473-m474.
17. Diop, M. B., Diop, L., Plasseraud, L., Maris, T. (2015). Crystal structure of 2-methyl-1H-imidazol-3-ium aquatrichlorido (oxalato- κ^2O, O′) stannate(IV). Acta Crystallogr. E71, 520-522.

18. Diop, M. B., Diop, L., Plasseraud, L., Cattey, H. (2016). Triorganotin carboxylates – synthesis and crystal structure of 2-methyl-1H-imidazol -3-ium catena-O,O′-oxalato triphenyl stannane. Main Group Met. Chem. 39, 119-123.
19. Diop, M. B., Seck, G. A., Sarr, M., Diop, L., Oliver, A. G. (2020). Co-crystallization of Oxalate Salts of Monoprotonated Amines with a Double Sn-Ph Bond Cleavage. Am. J. Het. Chem. 6, 16-23.
20. Vaidhyanathan, R., Natarajan, S., Rao, C. N. R. (2002). Hydrogen bonded structures in organic amine oxalates. J. Mol. Struct. 608, 123-133.
21. Apex2, Crystallographic Software, Suite, Bruker AXS Inc., Madison, Wisconsin (USA), (2013).
22. Apex3, Crystallographic Software, Suite, Bruker AXS Inc., Madison, Wisconsin (USA) (2015).
23. Saint (version 8.34A-2013), Area Detector Integration Software, Bruker AXS Inc., Madison, Wisconsin (USA), (2013).
24. Sheldrick G. M. (2008). A short history of SHELX. Acta Crystallogr. A64, 112-122.
25. Sheldrick G. M. (2015). Crystal structure refinement with SHELXL. Acta Crystallogr. C71, 3-8.
26. Spek, A. L. (2009). Structure validation in chemical crystallography. Acta. Crystallogr. D65, 148-155.
27. Macrae, C. F., Bruno, I. J., Chisholm, J. A., Edgington, P. R., McCabe, P., Pidcock, E., Rodriguez-Monge, L., Taylor, R., van de Streek, J., Wood, P. A. (2008). Mercury CSD 2.0 – new features for the visualization and investigation of crystal structures. J. Appl. Crystallogr. 41, 466-470.
28. Diop, M. B., Diop, L., Oliver, A. G. (2018). Acetonyltriphenyl phosphonium 2,3,5 triphenyl tetrazolium tetrachloridocuprate(II). Acta Crystallogr. E74, 69-71.
29. Asaji, T. (2018). Reorientation of diprotonated DABCO (1,4-Diazabicyclo[2.2.2]octane) cation and proton transfer in organic ferroelectric adduct DABCO-2(2-Chlorobenzoic acid). J. Mol. Struct. 1159, 174-178.
30. Sakurai, T., Saiki, R., Wei, R. J., Newton, G. N., Shiga, T., Oshio, H. (2016). Oxalate- bridged heterometallic chains with mono- cationic dabco derivatives. Dalton Trans. 45, 16182-16189.
31. Asaji, T., Shido, K., Fujimori, H. (2018). Reorientation of DABCO (1,4- diazabicyclo [2.2.2]octane) in halogen-bonded molecular complex DABCO-2(C_6F_5I). J. Mol. Struct. 1169, 81-84.
32. Wang, X.-F., Qi, X.-L., Shi, F.-N., Rocha, J. (2011). Syntheses, structures and properties of two cadmium compounds containing neutral or in situ protonized 1,4-diazabicyclo [2.2.2] octane. J. Mol. Struct. 1004, 26-30.
33. Quiles, F., Burneau, A. (1998). Infrared and Raman spectroscopic study of uranyl complexes: hydroxide and acetate derivatives in aqueous solution. Vib. Spectrosc. 18, 61-75.
34. Lermontov, A. S., Lermontova, E. Kh., Wang, Y. Y. (2009). Synthesis, structure and optic properties of 2-methylimidazolium and 2-phenyl imidazolium uranyl acetates. Inorg. Chim. Acta. 362, 3751-3755.
35. McCann, M., Curran, R., Ben-Shoshan, M., McKee, V., Devereux, M., Kavanagh, K., Kellett, A. (2013). Synthesis, structure and biological activity of silver(I) complexes of substituted imidazoles. Polyhedron. 56, 180-188.
36. Dhanabal, T., Sethuram, M., Amirthan Ganesan, G., Das, S. K. (2013). Spectral, thermal, structural, optical and antimicrobial activity studies on 2-methyl imidazolium picrate – An organic charge transfer complex. J. Mol. Struct. 1045, 112-123.
37. Barth, A. (2000). The infrared absorption of amino acid side chains. Prog. Biophys. & Mol. Biol. 74, 141-173.
38. Majoube, M., Millié, P., Vergoten, G. (1995). Vibrational spectra of 4-methylimidazole: assignment of modes and calculation of Raman and resonance Raman intensities at the ab initio 6-31G level. J. Mol. Struct. 344, 21-36.
39. Hasegawa, K., Ono, T., Noguchi, T. (2000). Vibrational Spectra and Ab Initio DFT Calculations of 4-Methylimidazole and Its Different Protonation Forms, Infrared and Raman Markers of the Protonation State of a Histidine Side Chain. J. Phys. Chem. B. 104, 4253-4265.

40. Baranowska, K., Piwowarska, N., Herman, A., Dolega, A. (2012). Imidazolium silanethiolates relevant to the active site of cysteine proteases. A cooperative effect in a chain of $NH^{+\cdots}S^{-}$ hydrogen bonds. N. J. Chem. 36, 1574-1582.
41. Effendy, Marchetti, F., Pettinari, C., Pettinari, R., Pizzabiocca, A., Skelton, B. W., White, A. H. (2006). Synthesis, spectroscopy and structural characterization of silver(I) complexes containing unidentate N-donor azole-type ligands. Inorg. Chim. Acta. 359, 1504-1512.
42. McCann, M., Curran, R., Ben-Shoshan, M., McKee, V., Tahir, A. A., Devereux, M., Kavanagh, K., Creaven, B. S., Kellett, A. (2012). Silver(I) complexes of 9-anthracenecarboxylic acid and imidazoles, synthesis, structure and antimicrobial activity. Dalton Trans. 41, 6516-6527.
43. Sow, Y., Diop, L. (2015). $R_2NH_2C_2O_4$ SnC_2O_4 $SnBu_3$, $(R_2NH_2)_4(C_2O_4)_3(SnR'_3)_2$ (R = Cy, i-Bu; R' = Me, Bu) and some mixed organo- and halotin (IV) oxalato new moieties containing complexes: Synthesis, Infrared, Mossbauer and NMR studies. Scientific Study & Research. 16, 123-131.
44. Coronado, E., Marti-Gastaldo, C., Galan- Mascaros, J. R., Cavallini, M. (2010). Polymetallic Oxalate-Based 2D Magnets: Soluble Molecular Precursors for the Nanostructuration of Magnetic Oxides. J. Am. Chem. Soc. 132, 5456 -5468.
45. Diop, M. B., Diop, L., Plasseraud, L., Cattey, H. (2016). Crystal structure of 2-methyl -1H-imidazol-3-ium hydrogen oxalate dihydrate. Acta Crystallogr. E72, 1113-1115.
46. Diop, M. B., Diop, L., Maris, T. (2016). Crystal structures of the two salts 2-methyl-1H-im idazol-3-ium nitrate–2-methyl-1H-imidazole (1/1) and 2-methyl-1H-imidazol-3-ium nitrate. Acta Crystallogr. E72, 482-485.
47. Diop, M. B., Diop, L., Plasseraud, L., Maris, T. (2016). Crystal structure of bis (2-methyl -1H-imidazol-3-ium)ihydroxidobis (oxalato-κ^2O^1,O^2)stannate (IV) monohydrate. Acta Crystallogr. E72, 355-357.
48. Callear, S. K., Hursthouse, M. B., Threlfall, T. L. (2010). A systematic study of the crystallisation products of a series of dicarboxylic acids with imidazole derivatives. Cryst EngComm. 12, 898-908.
49. Ndiaye, M., Diop, M. B., Samb, A., Diop, L., Oliver, A. G., Plasseraud, L. (2020). Bromide hydrogen oxalate salts with the diprotonated 1,4-diazabicyclo[2.2.2]octane counterion. Z. Naturforsch. B. doi:10.1515/znb-(2020)-0097.
50. Gong, H.-Y., Zhang, X.-H., Wang, D.-X., Ma, H.-W., Zheng, Q.-Y., Wang, M.-X. (2006). Methyl Zacali Pyridines: Remarkable Bridging Nitrogen-Tuned Conformations and Cavities with Unique Recognition Properties. Chem. Eur. J. 12, 9262-9275.
51. Cao, L.-H., Li, H.-Y., Xu, H., Wei, Y.-L., Zang, S.-Q. (2017). Diverse dissolution–recrystallization structural transformations and sequential Förster resonance energy transfer behavior of a luminescent porous Cd-MOF. Dalton Trans. 46, 11656-11663.
52. Kovalenko, E. A., Kochelakov, D. V., Samsonenko, D. G., Fedin, V. P. (2017). Crystal structure of binuclear bismuth complexes $[H_2dabco]_2[Bi_2Cl_{10}]\cdot 2H_2O$ and $(H_3O)_2$ $[H_2dabco]_4[Bi_2Br_{10}][BiBr_6]_2\cdot 4.5H_2O$. J. Struct. Chem. 58, 591-596.
53. Yutronic, N., Merchan, J., Gonzalez, G., Garland, M. T. (2002). Protonated bis (quinuclidine) included in layered bis (urea) –bromide and -iodide hosts, new ternary urea inclusion compounds. J. Chem. Soc. Perkin Trans. 2. 2, 1956-1959.
54. Thakur, T. S., Azim, Y., Srinu, T., Desiraju, G. R. (2010). N–H···O and C–H···O interaction mimicry in the 1, 1 molecular complexes of 5,5 diethylbarbituric acid with urea and acetamide N–H···O and C–H···O interaction mimicry in the 1, 1 molecular complexes of 5,5 diethylbarbituric acid with urea and acetamide. Curr. Sci. 98, 793-802.

Modular-Geometric Approach to Modeling the Process of Surface Microrelief Formation

E A Belki, V N Poyarkov & O I Markov

Oryol state University. I. S. Turgenev

ABSTRACT

Methods for modeling the microrelief of surfaces considered in the theory of shaping: flat, round, cylindrical, discrete-defined, etc. differ in their intended purpose. To evaluate the micro geometry of the surface layer of machined parts, which is carried out in order to match the shape of the microrelief of the performance details using known item parameters: All parameters are determined on a specific surface length from 0.1 to 25 mm. The parameters used to estimate the microrelief are one-dimensional. They allow us to represent the microrelief as a surface with numerical marks. A surface with numeric marks is a set of points whose coordinates are set in a three-dimensional Cartesian coordinate system. The law of location of points in space is not defined. A surface with numerical marks as a geometric image does not contain information about changes in geometric characteristics: the curvature in the normal section, the Riemann-Christoffel tensor, etc. which can be used to estimate its shape. The modular-geometric approach eliminates this problem.

Keywords: NA

Classification: FOR Code: 230111

Language: English

London Journals Press

LJP Copyright ID: 392962
Print ISSN: 2631-8474
Online ISSN: 2631-8482

London Journal of Engineering Research

Volume 21 | Issue 1 | Compilation 1.0

Modular-Geometric Approach to Modeling the Process of Surface Microrelief Formation

E A Belkin[α], V N Poyarkov[σ] & O I Markov[ρ]

ABSTRACT

Methods for modeling the microrelief of surfaces considered in the theory of shaping: flat, round, cylindrical, discrete-defined, etc. differ in their intended purpose. To evaluate the micro geometry of the surface layer of machined parts, which is carried out in order to match the shape of the microrelief of the performance details using known item parameters: All parameters are determined on a specific surface length from 0.1 to 25 mm. The parameters used to estimate the microrelief are one-dimensional. They allow us to represent the microrelief as a surface with numerical marks. A surface with numeric marks is a set of points whose coordinates are set in a three-dimensional Cartesian coordinate system. The law of location of points in space is not defined. A surface with numerical marks as a geometric image does not contain information about changes in geometric characteristics: the curvature in the normal section, the Riemann-Christoffel tensor, etc. which can be used to estimate its shape. The modular-geometric approach eliminates this problem.

Author α σ: Bolhov Plant of semiconductor devices Bolhov, 17, K. Marksa str., Oryol region, city of Bolkhov, 303140 Russia.
ρ: Department of Experimental and Theoretical Physics, Faculty of Physics and Mathematics, Oryol state University. I. S. Turgenev, 95, Komsomolskaya str., Orel 302026 Russia.

I. INTRODUCTION

The final formation of the microrelief of the surface of parts occurs at the stage of finishing processing operations according to the regulated parameters. Regulation of parameters is due to the need to match the formed microrelief to the type of wear of the functional surface of the part during its operation. The need to take into account the three-dimensional characteristics of the microrelief is particularly relevant in the manufacture of parts with specified performance properties, which are highly demanding in tribo-connections. It is known, for example, that wear resistance, fatigue strength and other operational properties are largely determined by the shape of the surface microrelief, namely, the curvature of the tops and depressions of micro-roughnesses. The part processing process is a single closed structure. One of the results of this process is the formed topography of the microrelief of the functional surface of the part [1].

Currently, each of the CAD models describing a separate side of the part processing process is based on the provisions of the scientific discipline that is directly studied by the phenomena under consideration. There is no General approach in the analytical description of the microrelief formation process. The calculation of the forming surface of the tool does not calculate the topography of the microrelief. This is due to the lack of sufficient information about the geometric structure of the microrelief as a three-dimensional image.

In order to improve the accuracy of the surface microgeometry estimation, you should additionally introduce geometric characteristics directly related to the surface curvature.

London Journal of Engineering Research

None of the used geometrical models of the micro-relief does not contain similar geometric characteristics. For example: in one-dimensional models, the height of micro-dimensions is used as the main geometric characteristic. In two-dimensional and three-dimensional models, characteristics that do not sufficiently contain information about the curvature of the local section.

Therefore, to date, there are no complete and well-founded three-dimensional geometric models of microrelief in the analytical description of the forming and processed surface.

The topography of a part's microrelief is usually evaluated after it is processed, rather than during the microrelief formation process. Methods of engineering geometry that allow you to link the curvature of a surface with its contact surface have not been developed [2].

Therefore, with a geometric representation of a microrelief, it is not possible to restore its structure with a sufficient degree of accuracy necessary to predict its topography and to control its geometric parameters during the part processing process [3]. Thus, the development of an approach to modeling the process of surface microrelief formation, which allows determining a system of geometric characteristics containing sufficiently complete information for evaluating the microrelief, is relevant [4,5].

II. THREE-DIMENSIONAL GEOMETRIC MODELS OF THE MICRORELIEF OF SURFACES CONSIDERED IN THE THEORY OF SHAPING

Three-dimensional geometric models of the microrelief of surfaces considered in the theory of shape formation are developed: flat, round cylindrical, frame discrete-defined and irregular-shaped bodies. The problem of calculating the coefficients of modules is formulated (table.4.) surface microrelief, in General: the surface is divided by the selected step along the z axis, the Cartesian coordinate system xyz, planes parallel to the XY plane, and a one-parameter family of surfaces. The step of splitting a family of surfaces is set by the family parameter.

The intersection points of the microrelief and families of parallel planes and surfaces are determined. At five points, the module – a local area of the surface-is restored as part of the surface of the contiguous paraboloid. The solution to the problem of calculating the coefficients of modules in the special case for a flat surface of the part is as follows:

Table 1: Determination of the type of module of a three-dimensional geometric model of a microrelief

№	Module view of a three-dimensional geometric model	The sign of the coefficients
1.	$k_1X^2+k_2Y^2 \geq -2Z;$	$k_1>0; k_2>0;$
2.	$k_1X^2+k_2Y^2 \leq -2Z;$	$k_1<0, k_2<0;$
3.	$k_1X^2+k_2Y^2 \geq 2Z;$	$k_1>0; k_2<0; (k_1<0, k_2>0);$
4.	$k_2Y^2 \geq -2Z;$	$k_1=0; k_2>0, (k_1=0, k_2<0);$
5.	$Z \leq 0;$	$k_1=0; k_2=0.$

In the global system of rectangular Cartesian coordinates, a field of points is defined by the values n on the X axis and the values m on the Y axis. For each point (x_i, y_j), $i=\overline{1,n}; j=\overline{1,m};$ the z_{ij} value is

known. (Figure 2.3) The x axis split step $\Delta x = (x_n - x_1)/n$. The y axis split step $\Delta y = (y_m - y_1)/m$. In the node - ($x_{i+1}; y_j; z_{k+1}$) at the base site L_x x L_y,

$$1 \le i \le n_x + 1, \quad 1 \le j \le n_y + 1, \quad 1 \le k \le (1 + n_x)(1 + n_y);$$

$$n_x = \frac{L_x}{\Delta x}, \quad n_y = \frac{L_y}{\Delta y},$$

determine the radii of curvature from the intersection points of real microrelief profiles R_{l1}, R_{l2} by three points in sections $x_{i+1}; y_j;$ (Figure 4.5). Based on Meunier's theorem, normal curvatures in sections are calculated $x_{i+1}; y_j;$

$$k_{1n} = \frac{\cos\varphi_1}{R_{l,1}}; \quad k_{2n} = \frac{\cos\varphi_2}{R_{l,2}};$$

Where φ_1 and φ_2 - angles between the main normal of the paraboloid and the normals of the arcs of circles in sections $x_{i+1}; y_j$.

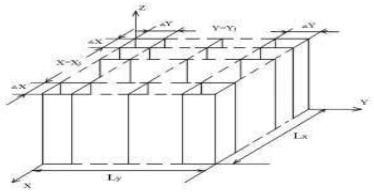

Figure 2: Model of splitting a microrelief mutually perpendicular planes

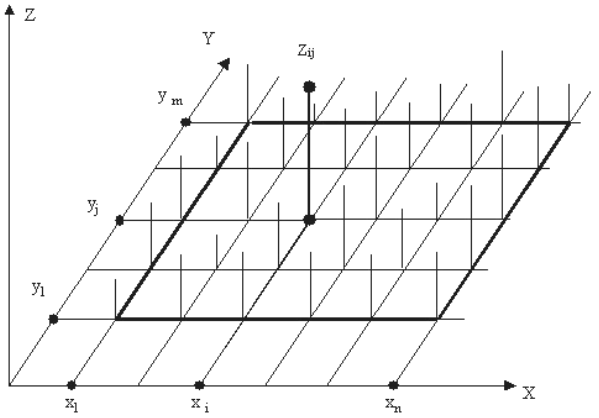

Figure 3: Initial data for calculating the microrelief with

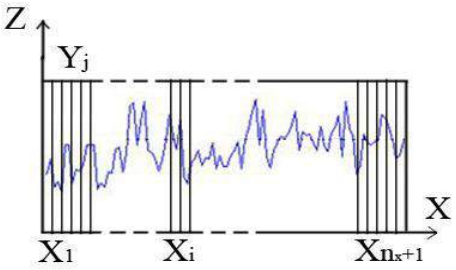

Figure 4: The breaking of the microrelief the in the plane $y = y_j$

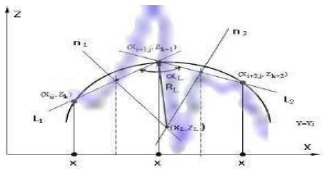

Figure 5: Diagram for calculating the radius of curvature in cross section $y = y_j$

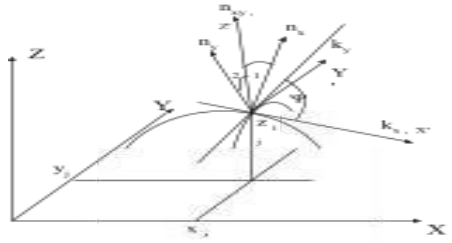

Figure 6: Normals and tangents

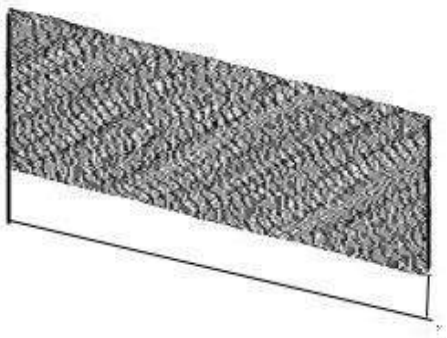

Figure 7: Modular geometric model of the microrelief of the 3x1. 5 mm surface of the sample after flat grindings: (scanning step 10 microns)

Assume that the normal curvature in one of the sections is equal to the main curvature $k_1 = k_{1n}$, the main curvature is determined by the Dupin's indicatrix k_2 in a section perpendicular to the selected section. (Figure 6.7). By value k_1 and k_2 define the type of geometric model module in a local Cartesian rectangular coordinate system XYZ with the origin at the node -($x_{i+1}; y_j$).

Relative error allowed when determining the Gaussian curvature based on the choice of the main curvature:

$$\varepsilon = \left|\frac{\Delta K}{K_1}\right| 100\% = \left|\frac{\left(k_{1n}^2 - k_{2n}^2\right) ctg^2\psi}{k_{1n}\left(k_{2n} - k_{1n}\cos^2\psi\right)} \sin^2\psi\right| 100\% = \left|\frac{\left(k_{1n}^2 - k_{2n}^2\right)\cos^2\psi}{k_{1n}\left(k_{2n} - k_{1n}\cos^2\psi\right)}\right| 100\%,$$

Where

$$\Delta K = K_2 - K_1 = \left(k_{1n}^2 - k_{2n}^2\right) ctg^2\psi \ ,$$

Based on the study of the equation, it is obtained:

If $\psi = \frac{\pi}{2}$, that $\varepsilon = 0$ and $K_1 = K_2$, I. e. k_{1n} and k_{2n} - are normal curvatures.

If ε - a pre-set value, then changing the steps of dividing the microrelief by parallel planes on the area $L_x x L_y$ on axes X and Y, you can determine the appropriate angle value ψ .

III. METHODS FOR NUMERICAL CALCULATION OF MICRORELIEF OF VARIOUS SURFACES

Methods have been developed for numerical calculation of the microrelief of surfaces: flat (Figure 8), round cylindrical, discrete-defined frame and irregular body [6,7].

The method of numerical calculation of the microrelief of a round cylindrical surface: for example, a PP grinding wheel (straight profile) allows you to determine the microrelief of the forming surface. The microrelief of the surface of the PP grinding wheel in the framework of a modular geometric model is a set of cutting edges of abrasive grains embedded in the tool bundle on its surface.

Step of splitting by parallel and radial planes of the microrelief on the side surface of the circular cylinder (on the periphery of the grinding wheel) along the axis z: Δz , by coordinates φ : $\Delta\varphi$. (Figure 9).

Radial planes – a bundle of planes whose axis is the axis z. Number of parallel planes (each plane is parallel to the plane z=0: i;

$$n_z = \frac{h}{\Delta z}, \text{ then: } 1 \le i \le n_z + 1, \ (n_x \text{ - even}),$$

Number of radial planes: j;

$$n_\varphi = \frac{2\pi R}{\Delta \varphi}, \text{ then: } 1 \le j \le n_\varphi + 1, (n_\varphi \text{ - even}),$$

Numerical calculation of the coefficients of contiguous paraboloids is performed using a method developed for structuring a three-dimensional geometric model of a flat surface microrelief.

The coordinates of the vertices of contiguous paraboloids are defined in a cylindrical coordinate system. The modular geometric model of the microrelief of the forming surface of the grinding wheel allows us to give a fairly complete assessment of the cutting ability of the tool.

The method of numerical calculation of the microrelief model of a frame discrete-defined surface: for example, the pen of a gas turbine blade includes a three-dimensional geometric model of the pen, structured on the basis of a smooth cross-linking of oblique helicoids.

It is known that the analytical task of the pen of a gas turbine blade in the framework of a three-dimensional geometric model: (Figure 10)

$$x_i \sin k_i z_i + y_i \cos k_i z_i = (l_i z_i + p_i)(x_i \cos k_i z_i - y_i \sin k_i z_i)^2$$

$$0 \le z_i \le h, k_i = \frac{\alpha_{im}}{h_i}, l_i = \frac{p_{im} - p_i}{h_i}$$

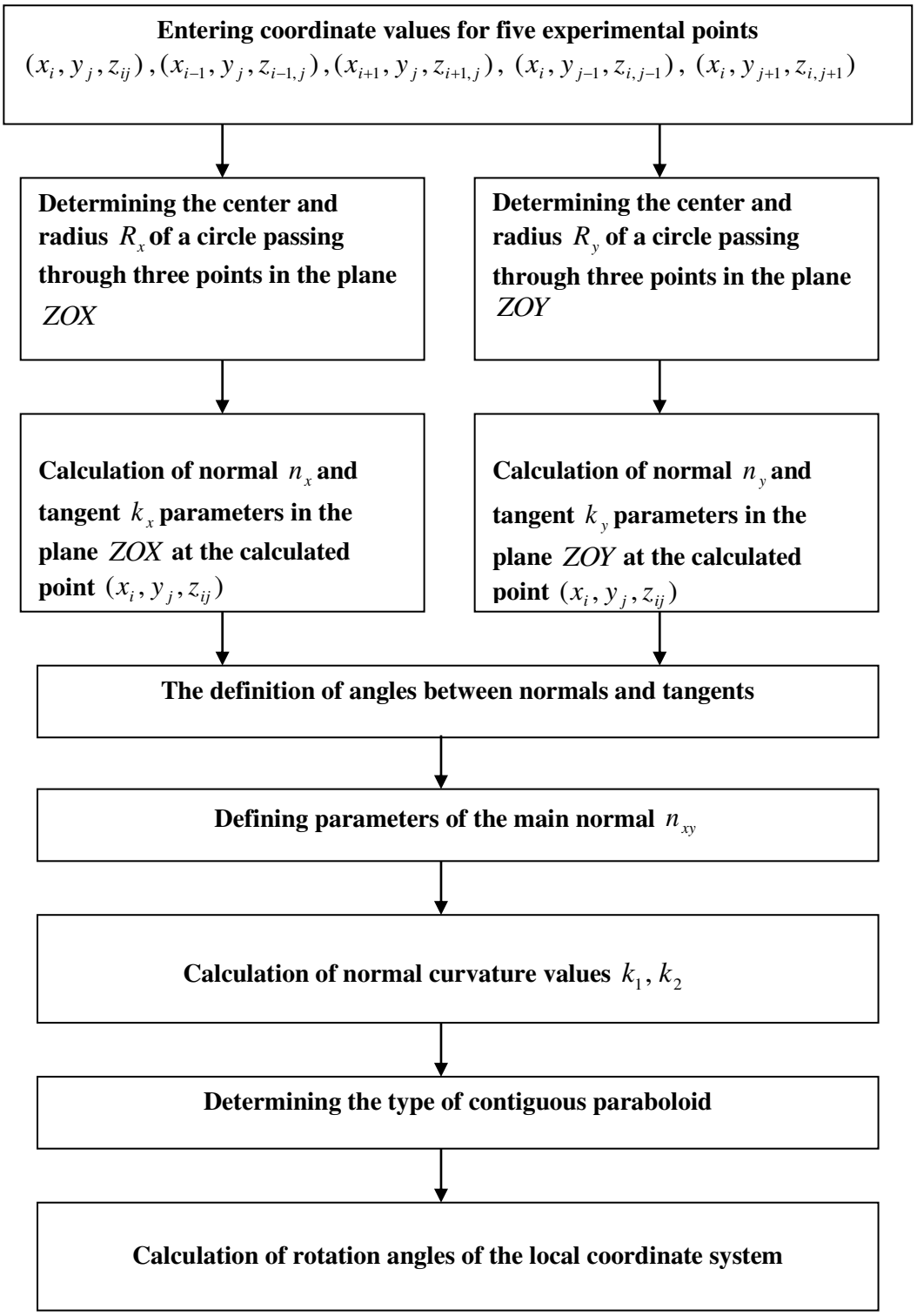

Figure 8: Block diagram for calculating paraboloid parameters of a three-dimensional geometric model at the design point (x_i, y_j, z_{ij})

Where $i = \overline{1,n}$ - module number of the oblique helicoid approximating the blade feather, α_{im} - maximum rotation angle of the coordinate system $x_i y_i$ relative to the origin.

London Journal of Engineering Research

p_{im} – the parameter of the parabola $y_{im} = p_{im} x_{im}^2$,

p_i - the parameter of the parabola $y_i = p_i x_i^2$,

h_i – height of the oblique helicoid with the number i.

For mathematical modeling of the pen's microrelief, a parallel plane partition of an oblique helikoid with a number i, is used on axis z_i Δz_{ij}, where $j = \overline{1,m}$ - number of the plane parallel to the plane $x_i y_i$. In the case of a one - parameter family of oblique helicoids with a common line of contact-the z_i axis, we consider the splitting of the microrelief profile in the plane with the number j by the family of parabolas

$$y_{ij} = p_{ij\beta} x_{ij}^2 + \beta \Delta y \tag{1}$$

Where Δp - step of splitting a family of parabolas by parameter p_{ij}, i.e. $\Delta p = p_{ij1} - p_{ij} = \ldots = p_{ij\beta+1} - p_{ij\beta} = \ldots = p_{ijM} - p_{ijM-1}$ - step of splitting the family of parabolas along the axis y_{ij}, Δy <0, $\beta = \overline{1,M}$.

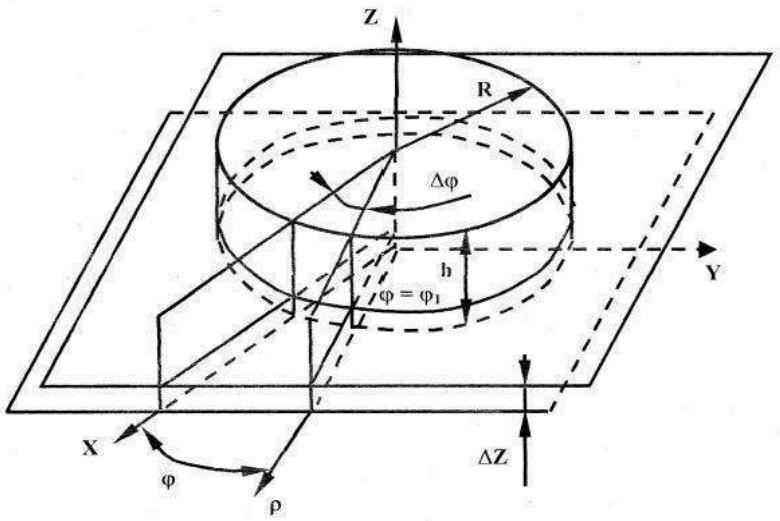

Figure 9: Model of splitting the microrelief of the periphery of the grinding wheel with mutually perpendicular planes

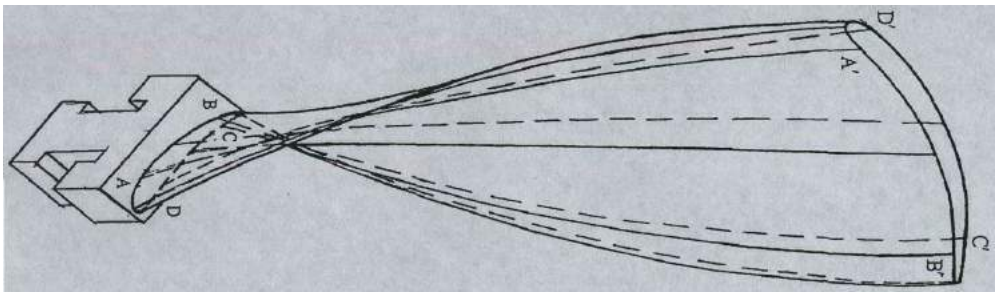

Figure 10: Modular-geometric model of a gas turbine blade ADA'D', ABA'B', BCB'C', CDC'D ' - modules-oblique helicoids

The $x_{ij}y_{ij}$ coordinate system is derived from the $x_i y_i$ coordinate system by turning an angle α_{ij} in the $x_i y_i$ plane and moving parallel along the z_i axis. The coordinates of the vertices of contiguous paraboloids are defined in a curved coordinate system $x_{ij}y_{ij}$. The coordinates of the vertex of the contiguous

London Journal of Engineering Research

paraboloid are determined in terms of the distances S_{ijA} from the origin to the point of intersection of the microrelief-A in the plane with the number j with the parabola from the family (1).
Relations for determining the abscissa and ordinate of point A:

$$x_{ijA} = \frac{1}{2p_{ij}}\left[\left(3p_{ij}S_{ijA}+1\right)^{2/3}-1\right] \quad y_{ijA} = p_{ij}x_{ijA}^2 = \frac{1}{4p_{ij}}\left[\left(3p_{ij}S_{ijA}+1\right)^{2/3}-1\right]^2$$

,

Known methods of numerical calculation do not allow us to determine the topography of the microrelief of the processed frame discrete-defined surface [8].

The method of numerical calculation of the microrelief of an irregularly shaped body: for example, an abrasive grain allows us to obtain qualitatively new results in the mathematical description of its surface; the surface of an abrasive grain is represented as a three - dimensional geometric image-a set of modules that have a non-smooth "cross-linking"; each surface module has an analytical representation in the local coordinate system associated with its vertex.

IV. SIMULATION MODEL OF FLAT SURFACE MICRORELIEF FORMATION

Developed a simulation model of microrelief flat surface depending on the processing modes, for example, flat grinding, which takes into account the changing topography of the surface microrelief of the workpiece depending on the angular speed of rotation of the circle, the speed of part motion, from the time of processing and the depth of grinding.

Parametric setting of a contiguous paraboloid

$$x = -\frac{2}{k_1 t_2}; \quad y = -\frac{2}{k_2 t_1}; \quad z = -2\left(\frac{1}{k_2 t_1^2}+\frac{1}{k_1 t_2^2}\right); \text{ где } t_1, t_2 \in (-\infty,+\infty)$$

The analytical definition of the surface formed by a contiguous paraboloid in the relative motion of an abrasive tool can be obtained from the matrix equation [9]:

$$\begin{pmatrix} x \\ y \\ z \\ 1 \end{pmatrix} = \begin{pmatrix} \cos wt & 0 & \sin wt & -vt \\ 0 & 1 & 0 & y_0 \\ -\sin wt & 0 & \cos wt & z_0 \\ 0 & 0 & 0 & 1 \end{pmatrix} \begin{pmatrix} x_1' \\ y_1' \\ z_1' \\ 1 \end{pmatrix}$$

where from : $x = x_1' \cos wt + z_1' \sin wt - vt = \chi_1;\ y = y_1' + y_0 = \chi_2;\ z = -x_1' \sin wt + z_1' \cos wt + z_0 = \chi_3;$

where: xyz – coordinate system related to the item, y_o =R – radius of circle, w is the angular velocity of the circle, v the velocity of the center of the circle relative items, t – time of motion of the circle relative to the details, $x = x_0 = -vt; y = y_0; z = z_0$ the vector of the shift of the beginning of the coordinate system relative to the beginning of the coordinate system xyz, $x_1' = x_1, y_1' = -z_1, z_1' = y_1.$ (Figure 11)

The matrix equation was derived from the General affine space mapping equation considered in the theory of surface shaping by cutting.

Equations for setting a contiguous paraboloid in the $x_1y_1z_1$ coordinate system associated with a circle:

$$x_1 = -\frac{2}{k_1 t_2}\cos(\varphi_{j+1}+\alpha_1)\cos\beta_1 + \frac{2}{k_2 t_1}\sin(\varphi_{j+1}+\alpha_1) + 2\left(\frac{1}{k_2 t_1^2}+\frac{1}{k_1 t_2^2}\right)\cos(\varphi_{j+1}+\alpha_1)\sin\beta_1 + x_{1,j+1};$$

$$y_1 = -\frac{2}{k_1 t_2}\sin(\varphi_{j+1}+\alpha_1)\cos\beta_1 - \frac{2}{k_2 t_1}\cos(\varphi_{j+1}+\alpha_1) + 2\left(\frac{1}{k_2 t_1^2}+\frac{1}{k_1 t_2^2}\right)\sin(\varphi_{j+1}+\alpha_1)\sin\beta_1 + y_{1,j+1};$$

$$z_1 = -\frac{2}{k_1 t_2}\sin\beta_1 - 2\left(\frac{1}{k_2 t_1^2}+\frac{1}{k_1 t_2^2}\right)\cos\beta_1 + z_{1,i};$$

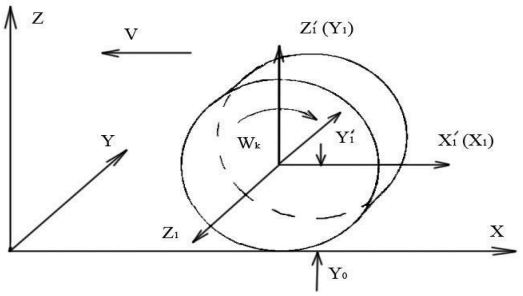

Figure 11: Converting the coordinate system $x_1 y_1 z_1$ of the grinding wheel to a new coordinate $x'_1 y'_1 z'_1$: W_K is the angular velocity of the V -is he speed of the circle in the coordinate system xyz

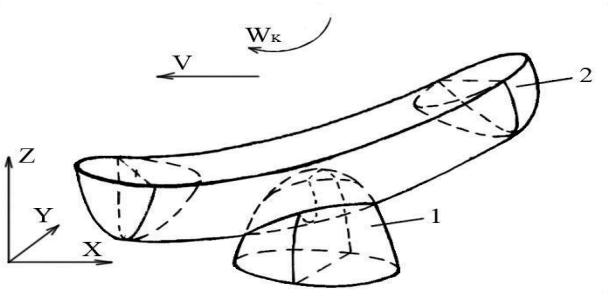

Figure 12: Scheme of forming the part system microrelief module for one pass circle, of the circlemicrorelief module:
1-part microrelief module,
2-circle microrelief module

Where : is the angle φ_{j+1} defining the corresponding j+1 radial plane. The plane passes through the xis of rotation of the circle; z_1, $x_{1,j+1}$;$y_{1,j+1}$,$z_{1,I}$ – coordinates that define the vertex of the touching araboloid in the coordinate system $x_1y_1z_1$, i- number of the plane parallel to the plane z_1=0, α_1, β_1 - otation angles when moving from the coordinate system $x_1y_1z_1$ to the coordinate system associated with he vertex of the touching paraboloid.

he surface of a contiguous paraboloid-as a module of the microrelief of the part surface in the xyz oordinate system is set as follows:

$$x = -\frac{2}{k_3 t_4}\cos\alpha_2 + \frac{2}{k_4 t_3}\sin\alpha_2\sin\beta_2 + 2\left(\frac{1}{k_4 t_3^2}+\frac{1}{k_3 t_4^2}\right)\sin\alpha_2\cos\beta_2 + x_{i+1} = \psi_1 \quad , \quad 1470 \ ,$$

$$z = -\frac{2}{k_3 t_4}\sin\alpha_2 - \frac{2}{k_4 t_3}\cos\alpha_2\sin\beta_2 - 2\left(\frac{1}{k_4 t_3^2}+\frac{1}{k_3 t_4^2}\right)\cos\alpha_2\cos\beta_2 + z_{k+1} = \psi_3$$

.

here k_3, k_4 - are the main curvature, t_3, $t_4 \in (-\infty,+\infty)$, x_{i+1}, y_j, z_{k+1} – coordinates that define a vertex of the osculating paraboloid in the coordinate system xyz, α_2, β_2 , the angles of rotation at the transition from coordinate system xyz to coordinate system connected with the top of the osculating paraboloid. Module flat microrelief of the workpiece surface after material removal module of the microrelief of the

iphery of the circle is determined from the condition: $\chi_1 \le x \le \psi_1$, $\chi_2 \le y \le \psi_2$, $\chi_3 \le z \le \psi_3$. (Figure 12).

The proposed geometric model of abrasive processing (the case of flat grinding) takes into account the actual location and geometric shape of the abrasive grains on the surface of the circle, the depth and width of the groove from the grains, the overlap of the grooves during grinding, as well as the real topography of the microrelief of the planes of the surface of the part. (Figure 13).

A three-dimensional geometric model of an abrasive tool-an abrasive grain, is presented as a non-smooth "cross-linking" of contiguous paraboloids, which allows you to analytically describe the macro geometry and microrelief of the abrasive grain. Thus, within the framework of one model, the geometric shape of the grain - in General, the cutting edges and the microrelief-is unambiguously estimated [10].

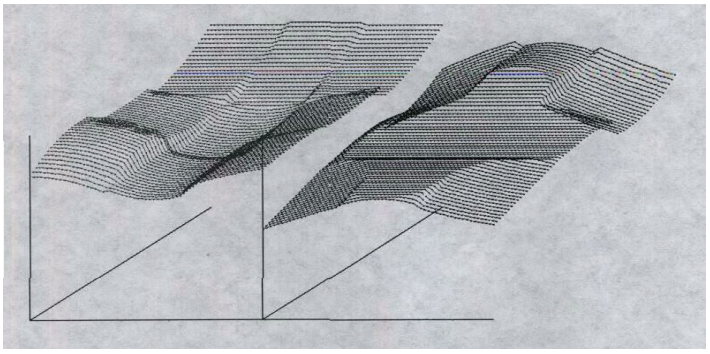

Figure 13: Formation of the microrelief of the surface layer of the part as a result of interaction with the microrelief of the abrasive tool

V. SETTING UP A HOLOGRAPHIC CONTROL (UGC)

Modern monitoring devices are designed in such a way that recording devices record parameter values from contour maps of an object. Contour maps are determined either with large errors, or for a sufficiently long time interval [11]. It is not possible to control a hard-to-reach object – an abrasive grain moving in the part material. There is one way to expand the capabilities of monitoring devices and use the information obtained with their help to build three-dimensional models, the use of devices that study the holographic image of an object.

One of these devices is the installation of holographic control (UGC) [12].

The principle of control of the installation under consideration is based on recent studies of the processes of obtaining a holographic image of an object in the optical and x-ray ranges. They allow you to study processing processes not in a projection on a plane, but in space.

The goal of the proposed device is to ensure the magnification, accuracy, and measurement capability of the reconstructed holographic image of the microrelief of the controlled object. This is achieved by the fact that in a profilograph containing laser beam splitters, optical converters, recording media-thick-layer emulsions, while increasing the three-dimensional interference pattern is carried out by a microscope, when recording and copying a holographic image of the surface microrelief, and an electromagnetic field indicator is used for measurements.

VI. CONCLUSION

Theoretical foundations and methods of geometric modeling of surface microrelief formation based on the Riemann-Christoffel tensor are Developed. A General approach is proposed that makes it possible to make a qualitatively new transition to the use of three-dimensional geometric models in the study of the process of forming a surface microrelief, which have optimal parameters that provide the most complete account of technological factors that affect the operational properties of the part.

Developed: methods of the modular-geometric approach that allow using three-dimensional geometric models to analytically describe the process of forming the surface microrelief and software packages that implement algorithms of the modular-geometric approach [13].

The problem of constructing a three-dimensional geometric model describing the surface microrelief based on the modular principle of structuring a complex surface shape is Solved. An analytical representation of a contiguous paraboloid through the main curvatures of the surface k_1,k_2, is obtained, which makes it possible to make a numerical calculation of a three-dimensional geometric model of the surface microrelief. In contrast to the well-known models for describing microrelief, this approach allows you to Supplement the frame model at the nodes by restoring the curvature of the surface in the sense of Riemann-Christoffel. The main characteristic of the microrelief topography is the Riemann-Christoffel tensor.

A new set of criteria is proposed: k_1,k_2 – the main curvature of the surface, Rz-the height of the micro-roughness, for the quantitative assessment of the surface microrelief, in contrast to the known criteria that allow for a mostly qualitative assessment of the microrelief. The hypothesis about the completeness of the proposed set of criteria was experimentally confirmed. It is recommended to use a method for evaluating the surface microrelief, which makes up for the lack of information about the geometry of the object, which is typical for classical methods of evaluating the microrelief.

The developed technique of numerical calculation of the surface microrelief: Methods for a flat surface, which allows, in contrast to known techniques to obtain the topography of the relief is to provide relief as a three-dimensional geometrical image is a set of modules of different types osculating paraboloid having a regulated "sshivku". The method for a circular cylindrical surface-a grinding wheel of the PP type (direct periphery), in contrast to the known mathematical models, allows us to give a fairly complete assessment of the cutting ability of the tool. An irregularly shaped body is an abrasive grain, which, within the framework of a single mathematical model of three-dimensional geometry, allows you to analytically describe with high accuracy the geometry of the grain as a whole and the geometry of its cutting edges [14].

A simulation model of the formation of a microrelief based on the specified geometric characteristics has been Developed. New equations are derived for the analytical representation of the surface formed by contiguous paraboloids in the relative motion of the tool. In contrast to the well-known equations of the part and tool profile that describe flat geometric models of processing, they contain fairly complete, in terms of geometric concepts, information about changes in the geometry and microgeometry of the forming and processed surface depending on the processing modes, tool installation parameters, etc [15].

REFERENCES

1. Avrutin Yu. D. Description of the relief of the working surface of the grinding wheel and analysis of the process of forming the grinding surface. In: Proceedings of VANISH, No. 14, L., 1973, pp. 27-39.
2. Druzhinsky I. A. Complex surfaces: mathematical description and technological support: Handbook. - L.: mechanical engineering. Leningr. otd-nie, 1985. - 263 p.

3. Borisov S. V., Nasonov D. I. Mathematical and graphic modeling of shaped cutting tools for processing complex surfaces of stamps and molds //"Design and technological Informatics" - KTI-96: Tr. 3-its Intern. Moscow: MSTU "Stankin", 1996, Pp. 32-33.
4. Bilik sh. M. Macrogeometry of daily machines. M., Mashgiz, 1962, p. 275.
5. lashnev S. I. Geometric model of forming surfaces with cutting tools/S. I. Lashnev, A. N. Borisov// STIN. -1995. -№ 4. -Pp. 22-26.
6. P. Germain-Lacour. Math and CAD: in 2 books. book 2. Pen. with Franz. [Germain-Lacour P.], Georges P. L., Pistol F., Bezier P.-M. Mir, 1989. - 264 P.
7. Nartya V. I. Building a system of mathematical models of complex surfaces / V. I. Nartya, Yu. K. Rebane / / Machines and tools. - 1993. - № 2. - Pp. 6-10.
8. Zavyalov Yu. S., Leus V. A., Skorospelov V. A. Splines in engineering geometry. - Moscow: Mashinostroenie, 1985. - 224 p.
9. Perepelitsa B. A. Maps of affine space in the theory of forming surfaces by cutting / B. A. Perepelitsa. - Kharkiv: Vyshcha school. Publishing house of Kharkiv. UN-te, 1981. - 152 p.
10. Mathematics and CAD: In 2 kN. KN. 1. Per. s Frantz. / schenen P., Kosnar M., Gardan I. et al. - M.: Mir, 1988. - 204 p.
11. Radzevich S. P. Forming complex surfaces on CNC machines / S. p. Radzevich. - Kiev "Vyshcha SHKOLA". 1991. - 192 p.
12. Pat. RF No. 2215317. Profilograph / Stepanov Yu.S., Belkin E.A., Barsukov G.V. Appied: 08.01.2002. Published:27.10.2003. Bull. 30.
13. Holographic image of the surface layer for 3D modeling. New method of non-destructive testing. LAP LAMBERT Academic Publishing. 2018. Belkin E. A., Poyarkov V. N., Markov O. I. P. 61.
14. New technologies of surface treatment of complex shape and control over its Geometry and topography of the microrelief. International journal of innovative studies and engineering technology. Volume 5, Issue: 4, 2019. E.A. Belkin, V.N. Poyarkov, O.I. Markov. P. 9-16.
15. Holographic devices for 3-D control over a complex surface shape. American Science Journal. №(34)/2020, Vol.2, E.A. Belkin, V.N. Poyarkov, O.I. Markov. P. 4-8.

Prevalence of Covid-19 Pandemic: A Paradigm Shift to Hydrogen Economy

Muhibbu-din Eniola Ismail

University of Ilorin

ABSTRACT

Covid-19 pandemic lockdown has slowed down the world economic system. The pandemic has cleared the roads, close factories and grounded planes causing severe economic challenges. The damaging impact of the pandemic amid lockdown has been a blessing in guise for the environment because of a significant drop in pollution level as transport and industrial sectors shutdown. Transport and industrial sectors are major contributors to environmental degradation through various emissions as a result of fossil fuel consumption. Energy consumed by transport and industrial sectors will have to shift to viable, readily available, economically and environmentally friendly with no carbon build up post Covid-19 pandemic. Hydrogen energy remains the best alternative option for technologies containing greenhouse gas emission and pollution of several forms. Hydrogen holds the potential to provide a clean, reliable, renewable and economical source of energy for meeting the growing and unending global energy needs post pandemic. The present paper explores the economic feasibility and potential of hydrogen to serve as a competitive fuel option post pandemic. In this paper, the role of hydrogen as an energy carrier hydrogen econo- my structure, potential of hydrogen economy, hydrogen production methods, hydrogen application and the economic and environmental importance of hydrogen as a viable fuel option post covid-19 pandemic were discussed. There will be a surge in demand and investment for hydrogen economy post Covid-19.

Keywords: corona virus; environmental degradation- on; hydrogen economy; clean energy; renewable sources; non renewable sources; economic impact; environmental impact.

Classification: FOR Code: 850399

Language: English

London Journals Press

LJP Copyright ID: 392963
Print ISSN: 2631-8474
Online ISSN: 2631-8482

London Journal of Engineering Research

Volume 21 | Issue 1 | Compilation 1.0

Prevalence of Covid-19 Pandemic: A Paradigm Shift to Hydrogen Economy

Muhibbu-din Eniola Ismail

ABSTRACT

Covid-19 pandemic lockdown has slowed down the world economic system. The pandemic has cleared the roads, close factories and grounded planes causing severe economic challenges. The damaging impact of the pandemic amid lockdown has been a blessing in guise for the environment because of a significant drop in pollution level as transport and industrial sectors shutdown. Transport and industrial sectors are major contributors to environmental degradation through various emissions as a result of fossil fuel consumption. Energy consumed by transport and industrial sectors will have to shift to viable, readily available, economically and environmentally friendly with no carbon build up post Covid-19 pandemic. Hydrogen energy remains the best alternative option for technologies containing greenhouse gas emission and pollution of several forms. Hydrogen holds the potential to provide a clean, reliable, renewable and economical source of energy for meeting the growing and unending global energy needs post pandemic. The present paper explores the economic feasibility and potential of hydrogen to serve as a competitive fuel option post pandemic. In this paper, the role of hydrogen as an energy carrier hydrogen economy structure, potential of hydrogen economy, hydrogen production methods, hydrogen application and the economic and environmental importance of hydrogen as a viable fuel option post covid-19 pandemic were discussed. There will be a surge in demand and investment for hydrogen economy post Covid-19.

Keywords: coronavirus; environmental degradation; hydrogen economy; clean energy; renewable sources; non renewable sources; economic impact; environmental impact.

Author: Department of Chemical Engineering, University of Ilorin.

I. INTRODUCTION

Since December 2019, there has been outbreak of novel coronavirus named covid-19 reported to have emerged from Wuhan in china. The disease continued to spread from China to many other part of the world, affecting 196 countries by March 25, 2020 (Chen et al., 2020; Xu et al., 2020). This spread aroused the attention of everyone worldwide. This transmission of the virus is from person to person through contacts influenced by environmental factors such as climatic conditions, population's concentration and medical quality (wang et al., 2020). In order to curtailed and controlled the spread of Covid-19, many cities in the world lockdown completely. Majority of roads, factories/industries and airports have been grounded in ordered to significantly reduce person to person contact and transmission. The consequent of the decision to lockdown resulted in dramatic improvement in the pollution level of air, water and soil quality. The global weather condition becomes better and the skies become blue and clearer. Covid-19 seems to be a blessing in disguise for the environment and implying that transport and industrial sectors are major contributors to global pollution. Transport and industrial sectors have a direct impact on global energy consumption. Restriction of both sectors have brought down current oil demand and consequently lowered green house gases. NASA satellite image have shown that pollutions level reduce remarkably in Chinese cities, western Europe, US, and Iran over the lockdown (Bauwens et al., 2020) and suggesting that there must be a paradigm shift in world energy demand for a cleaner and greener energy after the lockdown when transport and industrial

sectors will be opened. Therefore a shift toward hydrogen economy is inevitable. Hydrogen energy have the potential to redefine global energy landscape, providing options beyond oil and coal which have caused environmental degradation, issues on climate change and concerned for human health. Hydrogen economy will bring about a balance in economic goal, lower pollution level which can help the most vulnerable fight against future pandemic. Hydrogen energy is the best alternative energy to oil, coal and nuclear energy.

1.1 Hydrogen as energy carrier

Hydrogen is an abundant element on earth but not naturally occurring. Its combine with other element to form many common materials. It exists in water, hydrocarbon, coal, petroleum, natural gas, oil shale, biological material, carbohydrate, cellulose and protein. Hydrogen is not a primary energy source but alternative replacement to fossil fuel. With hydrogen energy technology, zero carbon footprint can be achieved from transport and industrial operations. As fascinating energy carrier, it can be produce from electricity and water. When combusted with oxygen, its form water and the water is return to nature. Little or no pollutants are generated or emitted. Currently, hydrogen is majorly produced as chemical feed stock. According to USDOE (2002)nine million ton of hydrogen are consumed annually in chemical production, petroleum refinery, metal treating and electrical applications in United States.

1.2 Hydrogen economy structure

Hydrogen economy is the system of production, distribution, consumption and utilization of hydrogen gas energy. It is composed of five segments: hydrogen production, storage, delivery, conversion and end-user applications. Fossil fuel, electricity and nuclear energy can be utilized to generate hydrogen through chemical, electrolytic, thermal and photolytic processes. Hydrogen can be stored as liquid or gas and be delivered to pipelines, trucks, trains, airplane and barges. With hydrogen gas as alternative energy air, water and soil quality will improve without any pollution as experienced during covid-19 lock-down.

1.3 Potentials of hydrogen economy

Currently energy sources are dominated by fossil fuels (coal, oil and gas) are considered as largest source anthropogenic emissions of greenhouse gas particularly carbon dioxide into the atmosphere that is largely responsible for global warming and climate change (Zanganeh and Shafeen, 2007). Increasing fossil fuel consumption has brought serious problems to the world including intractable energy security (Shaikh et al., 2016), greenhouse emission (Lin and Xu, 2018) and air pollution (Tilt, 2019). The impact of covid-19 around the world couple with global oil energy crisis, pollution and scarcity require the need to diversify and explore energy resources toward an alternative energy fuel. The alternative fuel must be clean, technically feasible, economically competitive, environmentally friendly, readily available (Meher et al., 2006) with no negative issues on human health and public welfare. Numerous potential alternative fuels have been proposed which include biodiesel, methanol, ethanol, hydrogen, boron, natural gas, liquefied petroleum gas (LPG), Fischer-Tropsch fuel, p-series, electricity and solar fuel (Mustafa Balat, 2008). Among all of these alternative fuels, hydrogen has the highest specific energy content of all conventional fuels (Campen et al., 2008) and is the most abundant element in the universe. Hydrogen economy is global solution to energy crisis/scarcity, air pollution health effects and global warming. Moreover hydrogen can be generated or regenerated from variety of energy sources like coal, nuclear, wind, solar energy. Hydrogen thus offers the promise energy security and availability through great production and use of domestic energy resources. Eventually the world will run out fossil fuels and at that time the society will be force to transition of alternative fuel of hydrogen. Most importantly application of hydrogen energy in transport sector through fuel cell vehicles and industrial sector will improve urban and industrial air quality thereby reduces generation of photochemical smog in urban/industrial environment. Since transport and industrial sectors are major contributor to climate change which result to global warming but with wide application of onboard hydrogen fuel cell technology on transport and industrial sectors,

zero emission will be achieve thereby hydrogen is a solution to global warming. Global market for hydrogen is already greater than $40 billion per year (Tilt, 2019). This include hydrogen used in ammonia production (49%), petroleum refining (37%), methanol production (8%), and miscellaneous smaller-volume uses (6%) (10). Present utilization of hydrogen is slightly above 3% of the energy consumption and with a growth rate estimated at 5–10% per year (Prince-Richard et al., 2005) It can be foresee and predicted that hydrogen energy demand production and consumption will increase after covid-19 pand- emic. Australia and Germany governments have made tremendous investment in hydrogen supply pre covid-19 pandemic (AREA, 2019) and more investment will be done by first world countries post covid-19 pandemic.

II. PROPERTIES OF HYDROGEN AS INDUSTRIAL AND TRANSPORT FUEL

Hydrogen is a colourless, odourless, tasteless gas and nontoxic gas found in the air at concentration of about 100 ppm (0.01%) (Suban et al., 2001). It is the lightest known substance: it is 14.4 times less dense than air. It is the most abundant element in the universe although in combine form, making up to 75% of normal matter by mass and over 90% by number of atoms (Mariolakos et al., 2007) To provide energy, hydrogen can be either burned or reacted chemically at very high conversion efficiency and will produce virtually little/no emissions. Like any other fuel source, hydrogen has both strengths and weaknesses based on its chemical and physical properties. Below are the properties of hydrogen compare to natural gas and gasoline as industrial and transport fuel:

Properties	Hydrogen	Natural Gas	Gasoline
Molecular weight (g/mol)	2.016	16.04	~110
Mass density (kg/$N_A m^3$) at P=1, T=0°C	0.09	0.72	720-780
Mass density of liquid H_2 at 20 K (kg/$N_A m^3$)	70.9	-	-
Boiling point (K)	20.2	111.6	310-478
Higher heating value (MJ/kg) (assumes water is produced)	142.0	55.5	47.3
Lower heating value (MJ/kg) (assumes steam is produced)	120.0	50.0	44.0
Flammability limits (% volume)	4.0-75.0	5.3-15.0	1.0-7.6
Detonability limits (% volume)	18.3-59.0	6.3-13.5	1.1-3.3
Diffusion velocity in air (m/s)	2.0	0.51	0.17
Ignition energy (mJ)			
At stoichiometric mixture	0.02	0.29	0.24
At lower flammability limit	10	20	not available
Flame velocity in air (cm/s)	265 325-	37-45	37-43
Toxicity	Nontoxic	Nontoxic	Toxic above 50 ppm

As an industrial and transport fuel option while considering environmental concerns, hydrogen exhibits numerous advantageous properties including its high diffusion velocity, highest heating value of any fuel (per kilogram), wide range of flammability and detonability limits, low ignition energy, high flame speed, and nontoxicity. Because hydrogen diffuses very rapidly, it will disperse quickly from a leak, and doesn't form puddles that can explode.

London Journal of Engineering Research

Table 1 show that the heating value of fuels, or the amount of heat that is transferred from the complete combustion of fuels in air increases with the hydrogen to carbon ratio (H/C).Thus, gasoline has the lowest heating value and hydrogen the highest, and therefore a very high potential to do useful work in an engine. The broad range of flammability and detonability limits of hydrogen (the concentration of the fuel in air that can ignite or explode respectively) means that hydrogen does not have to be in stoichiometric ratios to be combusted; it can be burned in leaner concentrations leading to reduce fuel consumption. In other words Hydrogen engines can be operated more effectively on excessively lean mixtures than gasoline engines. As little as 4% hydrogen by volume with air produces a combustible mixture (Norbeck et al., 1997) and Hydrogen can detonate over a very wide range of concentrations when confined, however, unlike many other fuels; it is very difficult to detonate if unconfined.

Additionally, the energy required to ignite a mixture of hydrogen in air is low at stoichiometric mixture and lower flammability limit, 0.02 and 10 MJ respectively. The flame speed of hydrogen is high, both factors which aid in the complete mixing and combustion of the fuel in a hydrogen combustion engine. The non toxicity of hydrogen is also an added bonus when compared to gasoline or any other fuel. When looked at with its environmental friendliness, except for very small levels of NOx, hydrogen produces only water when burned or chemically reacted. Its physical properties make it an intriguing fuel option. However, hydrogen also has several drawbacks. Compared to natural gas and gasoline, hydrogen is a very low-density diatomic gas, and thus must be compressed to very high pressures, liquefied at a temperature of about -252°C, or stored in some other specialized fashion in order to condense a reasonable amount in a reasonable volume. As a compressed gas, hydrogen exhibits rather low energy density, containing about one-third the energy as an equivalent volume of natural gas at the same pressure and as a cryogenic liquid, about one-third the energy as an equivalent volume of gasoline. Hydrogen is also an extremely small molecule, diffusing more readily than other fuels, and is more likely to leak. Moreover, it can even diffuse into some metals and cause embrittlement therefore hydrogen systems thus necessitate special materials considerations. The lower flammability limit of hydrogen, above considered as a strength, also means that if hydrogen leaks and builds up in low concentrations in an enclosed space, accidental explosion can occur or if fuel and air mix outside the cylinder of an engine, backfiring can occur. Due to a high flame velocity, this explosion could also travel very rapidly. A potential solution to backfiring is direct injection of hydrogen gas into the cylinder prior to spark generation which also increases engine efficiency by allowing the engine to run at higher compression ratios than if it ran on gasoline. Nonetheless, backfiring remains a potential risk of a hydrogen combustion engine. Hydrogen clearly exhibits several attractive physical properties when it comes to fuel applications, but it is also important to remember its potential risks when implementing it in a industries and transport sector.

Laboratory tests conducted on internal combustion engines burning hydrogen demonstrate good performance (Berry et al., 1996). In comparison with an engine burning gasoline, the emission of nitrogen oxides is far less for the engine-fueled hydrogen. The product of hydrogen combustion with air is water vapor and negligible pollution when the peak temperature is limited. Some oxides of nitrogen (NOx) are formed at very high combustion temperatures(<2300 K); fortunately, the auto ignition temperature of hydrogen is only 858 K (Plass Jr., et al., 1990). The oxide of nitrogen (NO_x) is form as a result of combustion of air with hydrogen mixture. The air is mixture of gases majorly 78% nitrogen and 21% of oxygen with very small amount of CO_2, noble gases and water vapour. Hydrogen has good properties as a fuel for internal combustion engines in automobiles. Some of the characteristic properties of a hydrogen–air mixture that can definitely influence the engine design and performance are low ignition energy, low ignition energy, low density, wide range of ignition limits, high diffusion speed, and high flame speed (Plass Jr., et al., 1990).

2.1 Sources of hydrogen

Hydrogen can be source from variety of primary energy such as fossil fuels, nuclear (Utgikar and Thiesen, 2006), solar (Charvin et al., 2008), wind (Granovskii et al., 2007), hydropower (Tarnay, 1985) and geothermal energy (Sigurvinsson et al., 2006). Different energy resources with various pathways can be utilized to generate hydrogen. Various processes such as methane steaming steam reforming, water electrolysis, high temperature electrolysis, and thermochemical cycles are available to produce hydrogen as well. The main sources for commercial production of hydrogen include natural gas (48%), oil (30%) coal (18%) and electrolysis (4%) of world hydrogen production (Press et al., 2008). Fossil fuels conversions are dominant source of commercial/ industrial hydrogen such as natural gas reforming (Häussinge et al., 2011).

With respect to production capacities, hydrogen production can also be categorized into 'distributed' or 'centralized' production. Distributed production facilities are smaller in scale and closer to the consumers. As such distributed generations can meet the demand from transportation sector of hydrogen powered fuel cell vehicles during the transition period to a hydrogen economy and once the market expands, the hydrogen production will be scaled up and 'centralized' to take advantage of economies of scale as well as the higher efficiency from larger scale production and to meet the greater amount of hydrogen demand in industrial sector.

III. Hydrogen Production Processes/Methods

3.1 Steam reforming of Natural Gas

Steam methane reforming (SMR) is a process in which the natural gas or other methane streams, such as biogas or landfill gas, reacts with steam in the presence of a catalyst (usually nickel) to produce hydrogen and carbon monoxide. It is worth mentioning that natural gas reforming produces for more than 90% of hydrogen production worldwide and remains the most commonly used method for hydrogen production. This process consists of heating the gas to between 700-1100 °C in the presence of steam and a nickel catalyst. The resulting endothermic reaction breaks up the methane molecules and forms carbon monoxide CO and hydrogen H_2 (Mazloomi & Gomes, 2012).

$$CH_4 + H_2O \rightarrow CO + 3H_2$$

The carbon monoxide gas can then be passed with steam over iron oxide or other oxides and undergo a water gas shift reaction to obtain further quantities of H_2.

$$CO + H_2O \rightarrow CO_2 + H_2$$

The downside to this process is that its major by-products are CO, CO_2 and other greenhouse gases. Depending on the quality of the feedstock (natural gas, rich gases, naphtha, and others), one ton of hydrogen produced will also produce 9 to 12 tons of CO_2.

According to the Director of Energy of USA (2010), SMR is approximately 72% efficient in hydrogen generation when starting with natural gas. Conversely, on a lower heating value basis. SMR produces a hydrogen-rich gas that is typically on the order of 70 – 75% hydrogen on a dry mass basis, along with smaller amounts of methane (2–6%), carbon monoxide (7–10%), and carbon dioxide (6–14%) (Sharma and Ghoshal, 2015).

In addition, SMR is not an attractive production route for a developed hydrogen economy. This is due to the fact that the order-of-magnitude increase in demand would deplete our finite reserves. Moreover, the concentration of gas reserves in relatively few regions of the world could lead to geopolitical tension and unstable supplies. Environmental impact is also a major concern because reforming natural gas to hydrogen produces as much pollution and CO_2 as burning the natural gas directly. Generation of hydrogen from natural gas is a well-established process. If sufficient quantities are produced to power the world's cars and light trucks it would strain the world's supply of conventional methane, making natural gas as geopolitically sensitive as an oil (Sharma and Ghoshal, 2015).

3.2 Gasification of coal and other hydrocarbons

Currently, gasification processes are mainly used in large-scale integrated gasification combined cycle power plants (due to the low flexibility of synthesis gas production) in order to supply base energy load. But in a short-term future, the possibility to produce hydrogen from syngas could make gasification technologies very interesting also for medium and small-scale industrial applications. To this aim, Sotacarbo, Ansaldo Ricerche, ENEA and the Department of Mechanical Engineering of the University of Cagliari developed an integrated gasification and syngas treatment process for combined production of hydrogen and electrical energy for medium and small-scale commercial applications (Deiana et al., 2007).

The partial oxidation process termed as "gasification", generates hydrogen from a wide range of hydrocarbon fuels, including coal, heavy residual oils, and low-value refinery products. In this process, the hydrocarbon fuel is made to react with oxygen in a less than stoichiometric ratio, yielding a mixture of carbon monoxide and hydrogen at 1200 to 1350°C (Sharma & Ghoshal, 2015). Coal is a practical option for making hydrogen in large plants. Worldwide coal reserves and commercially available technologies make coal a practical option for producing hydrogen in large plants. Compared to the existing methods (i.e. electrolysis), gasification is more suitable for converting coal to hydrogen(Acar and Dincer, 2014).

The process begins with partial oxidation, which means some air is added to the coal, which generates carbon dioxide gas through traditional combustion. Not enough is added, though, to completely burn the coal (only enough to make some heat for the gasification reaction). The partial oxidation also makes its own gasification agent, carbon dioxide. Carbon dioxide reacts with the rest of the carbon in the coal to form carbon monoxide (this is the endothermic gasification reaction, which needs heat input). No hydrogen yet.

Carbon monoxide in the gas stream is now further reacted with steam, generating hydrogen and carbon dioxide. Now we are making some hydrogen. The hydrogen can then be run through an on-site fuel cell to generate high-efficiency electricity. Brown coals are generally preferred for gasification over black coals for several reasons. The main reason is that, because of the high oxygen content of this type of coal, it is less chemically stable and therefore easier to break apart during the gasification reaction. Also, there is a small boost from the hydrogen that is already present in the coal (Allen, 2018).

Hydrogen produced from this method is not a zero-emission fuel. Carbon dioxide is generated through the combustion and thermal decomposition reactions and is also a by-product of the reaction between carbon monoxide and water to make hydrogen and carbon dioxide.

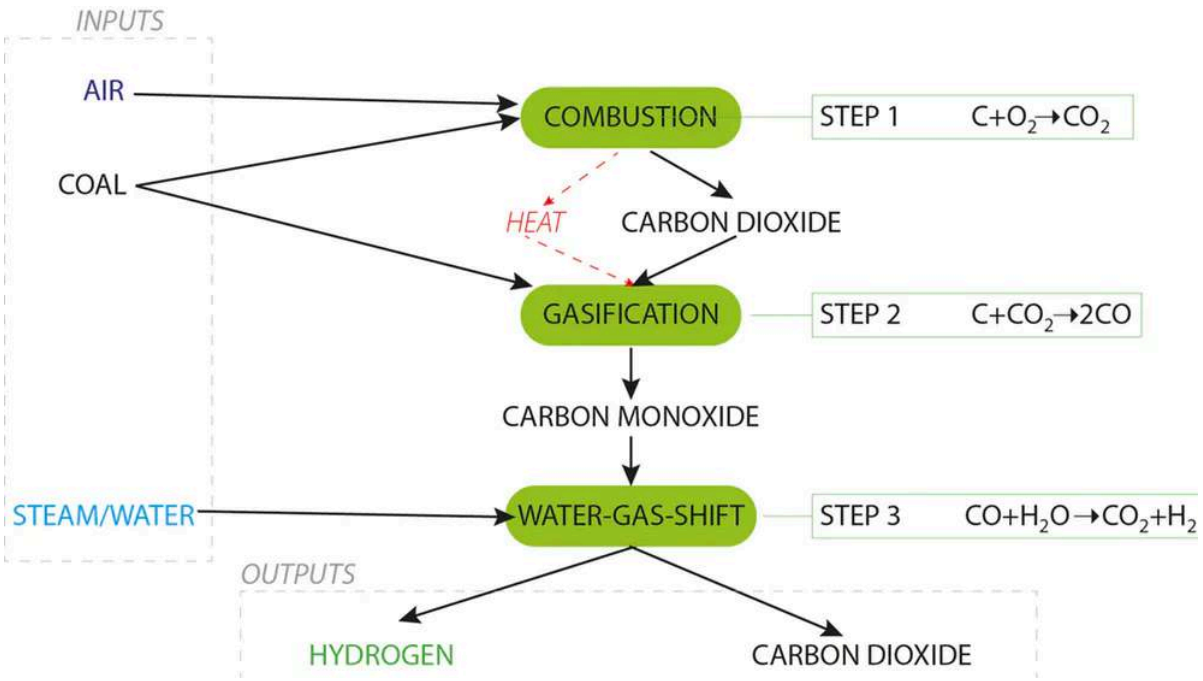

Production of Hydrogen from gasification of coal (Allen, 2018)

3.3 Hydrogen Production From Nuclear Energy

3.3.1 Hermochemical water splitting

Thermochemical water splitting uses high temperatures from nuclear power plant reactions to produce hydrogen and oxygen from water. Thermochemical water splitting processes use high-temperature heat (500°C or more) to initiate a series of chemical reactions that generate hydrogen. The chemicals used in the process are reused within each cycle, creating a closed-loop that uses up only water and produces hydrogen and oxygen.

Thermochemical water splitting cycles have a major advantage of not requiring catalysis to drive individual chemical reactions. Except for water, which is the material source of hydrogen production, all chemicals used in the thermochemical cycle can be recycled. Other advantages of thermochemical water splitting cycles are little or no need for $O_2 - H_2$ separation membranes, reasonable temperature requirement range of 300-1000°C and zero or low electrical energy requirement.

Being fully developed and demonstrated in Japan and the US, the S-I cycle (Sulfur-Iodine cycle) is considered as technically viable. Though there are numerous setbacks associated with this method of hydrogen production. The first reaction of S-I cycles is thermally driven and it can be written as:

$$H_2SO_{4(aq)} \xrightarrow{\text{Heat 300-500°C}} H_2O_{(gas)} + SO_{3(g)}$$

The product gases (H_2O and SO_3) are separated and heated up to 800-900C. Then SO_3 gas is decomposed thermally according to

$$SO_{3(g)} \xrightarrow{\text{Heat 800-900°C}} \frac{1}{2}O_{2(g)} + SO_{3(g)}$$

After separation from O_2, SO_2 undergoes an exothermic reaction with iodine and water which occurs at low temperatures spontaneously:

$$SO_{2(g)} + I_{2(g)} + 2H_2O_{(l)} \rightarrow 2HI_{(g)} + H_2SO_{4(aq)}$$

Lastly, HI thermally decomposes into H_2 at temperatures around 420-450°C:

$$2HI_{(g)} \xrightarrow{\text{Heat 425-450°C}} H_{2(g)} + I_{2(g)}$$

Since there are no side reactions happening during the S-I cycle, it is reasonably straight forward to separate and reuse the chemicals used in Reactions (3)-(6). Because of the relatively high reaction temperature requirements of S-I cycles, there are not many sustainable thermal energy sources available to drive the individual reactions in the cycle. Nuclear, concentrated solar, and biomass combustion heat can be listed as possible sustainable thermal energy sources to drive the S-I cycle reactions. In the hybrid version of S-I cycles, the hydrogen-generating reaction is supported electrochemically (Dincer and Acar, 2014).

3.4 Hydrogen Production From Renewable Energy

3.4.1 Biomass Gasification

Biomass sources such as wood and agricultural products, solid wastes, landfill gas and biogas, ethanol, biodiesel and so on can be processed for the production of hydrogen. Biomass conversion technologies are divided into two categories: thermo-chemical and biochemical processes. Thermochemical processes tend to be less expensive because they can be operated at higher temperatures and therefore achieve higher reaction rates. They involve either gasification or pyrolysis (heating biomass in the absence of oxygen) to produce a hydrogen-rich stream of gas known as "syngas" (a blend of hydrogen and carbon monoxide) (Sharma and Ghoshal, 2015). Though biomass gasification has not been able to produce hydrogen on a large scale at a competitive price. Nevertheless, this method could still be used to generate energy from domestic and agricultural waste in a clean way.

One method of generating hydrogen from biomass begins with processing the organic materials at high temperatures, but without combustion. When combined with oxygen and steam, the reaction results in carbon monoxide, carbon dioxide and hydrogen gas. This gasification process can take the carbon monoxide that is produced and combine it with additional steam to produce additional hydrogen and carbon dioxide, which is recycled through the natural plant respiration cycle and generate additional biomass. Alternative options may involve biological agents, such as anaerobic bacteria or fermentation, or pyrolysis, which uses the same gasification process, but without the presence of oxygen. Research in this field is suggesting new ways to improve efficiency and increase the implementation of hydrogen generation from biomass. Along with analysis that shows that biomass feedstock usable for energy production should be plentiful, the future usage of hydrogen production techniques related to biomass should continue to grow. Looking toward further opportunities, research being conducted promises to develop bacterial and microbial actors that increase production efficiency, while additional efforts focus on methods to lower both production costs and the costs of obtaining the feedstock.

3.4.2 Electrolysis (water-Electrolysis)

Water electrolysis is the process whereby water is split into hydrogen and oxygen through the application of electrical energy, as in Eq. (6). Typically, a water electrolysis unit consists of an anode, a cathode separated with an electrolyte, and a power supply. The electrolyte can be made of an aqueous solution containing ions, a proton exchange membrane (PEM) or an oxygen ion-exchange ceramic membrane. A direct current (DC) is applied from the negative terminal of the DC source to the cathode (seat of the reduction reaction), where the hydrogen is produced. At the anode, the electrons produced by the electrochemical reaction return to the positive terminal of the DC source.

For the case of water electrolysis in an acid aqueous electrolyte, the processes that occur at the anode and the cathode are described, respectively, by Eqs. 1 and 2:

$$H_2O \rightarrow \frac{1}{2}O_2 + 2H^+ + 2e^- E^0 \quad ---- \quad Eq\,1$$

$$2H^+ + 2e^- \rightarrow H_2E^0 \quad ---- \quad Eq\,2$$

The half-reactions occurring at the cathode and the anode respectively can be written as:

$$2H_2O + 2e^- \rightarrow H_2 + 2OH^- E^0 \quad ---- \quad Eq\,3$$

$$2HO^{-} \rightarrow \frac{1}{2}O_2 + H_2O + 2e^{-}E^{0} \quad =---- \; Eq\,4$$

The global reaction for the two cases is:

$$H_2O \rightarrow H_2 + \frac{1}{2}O_2 \qquad ---- \; Eq\,5$$

Electrolysis of water is not a spontaneous phenomenon because the standard global reaction potential is negative. Therefore, it needs an extra intervention (power source) and the global reaction can be written as:

$$H_2O + electricity \rightarrow H_2 + \frac{1}{2}O_2 \quad --- \; Eq\,6$$

Electrolysis of pure water requires excess energy in the form of overpotential to overcome various activation barriers. Without the excess energy, the electrolysis of pure water occurs very slowly or not at all. This is in part due to the limited self-ionization of water. Pure water has an electrical conductivity of about one-millionth that of seawater. Many electrolytic cells may also lack the requisite electrocatalysts. The efficiency of electrolysis is increased through the addition of an electrolyte (such as a salt, an acid or a base) and the use of electrocatalysts.

Water electrolysis has some unique qualities. Electrolysis could be used for hydrogen production at any place around the globe. The only requirements of this production are electricity and water where the production rate/capacity could be tuned for a certain demand at any place. With regard to the characteristics of water electrolysis, this method is capable of producing absolutely sustainable and clean hydrogen and also oxygen can be obtained for hospitals and world's water ways remediate hypoxia issues. This goal can be achieved only if the required electricity is obtained from an emission-free method such as wind, solar, geothermal systems, ocean wave or other renewable and green sources. (K. Mazloomi, 2012).

IV. HYDROGEN STORAGE

Hydrogen gas has a good energy density by weight, but poor energy density by volume against hydrocarbons; hence it requires a large storage facility. Storage of Hydrogen gas is one of the key regions where huge advancements are required to hasten the utilization of hydrogen in transportation, refining, power generation applications and in chemical industries. There are several ways of storing hydrogen, but the widely recognized methods are: High-pressure storage in the gaseous form, very low-temperature storage in the liquid form and hydride-based storage in the solid form.

4.1 Hydrogen stored as compressed gas in high-pressure tanks

The easiest way to decrease the volume of a gas, at constant temperatures, is to increase its pressure (Boyle's law). Storage of hydrogen gas typically requires high-pressure tanks (200 to 350 bar cylindrical tank pressure), although systems with at least 700 bar capacity are currently under development. These cylinders/tanks are being made from (i) steel (ii) Aluminum core encased with fibreglass and (iii) Plastic core encased with fibreglass. Compressed hydrogen storage systems have been demonstrated in hundreds of prototype fuel cell vehicles and are available commercially at low production volumes. While compressed hydrogen typically is stored at near-ambient temperatures, "cold" (sub-ambient but greater than 150 K) and "cryogenic" (150 K and below) compressed hydrogen storage are being investigated due to the higher hydrogen densities that can be achieved at reduced temperatures.

4.2 Hydrogen Stored as Liquid in tanks

Another industrial technique for storing maximum hydrogen in a restricted volume is to convert hydrogen gas to liquid hydrogen by cooling it to a very low temperature.

Hydrogen turns into a liquid when it is cooled to a temperature below -252. 87 °C. At -252.87°C and 1.013 bars, liquid hydrogen has a density of close to 71 kg/m^3. At this pressure, 5 kg of hydrogen can be stored in a 75-litre tank. In order to maintain liquid hydrogen at this temperature, tanks must be perfectly isolated. Currently, storing hydrogen in the liquid form is being reserved for certain special applications, in high-tech areas such as space travel.

4.3 Hydrogen stored as solid

The storage of hydrogen in solid form that is stored in another material is also a promising avenue of research. Methods for storing hydrogen in solid form are techniques involving absorption or adsorption mechanisms of hydrogen by a material. One example is to form solid metallic hydrides through the reaction of hydrogen with certain metal alloys. This absorption is the result of the reversible chemical combination of hydrogen with the atoms that comprise these materials. The most promising materials are composed of magnesium and alanates. Only a low mass of hydrogen can be stored in these materials, which is currently the major downside of this technology. In fact, the best materials currently generate a ratio of hydrogen weight to the total weight of the tank of not more than 2 to 3%. Before considering large-scale applications, it is also important to master certain key parameters such as kinetics (cell performance), the temperature and pressure of the charge and discharge cycles of hydrogen in these materials.

V. HYDROGEN APPLICATION

Vozniuk et al., 2019 revealed that hydrogen is one of the key starting materials used in the chemical industry with an annual worldwide production of about 50 million tons, currently, the largest amount (≈95%) of the total manufactured hydrogen is consumed mainly by two industrial segments: the chemical sector, accounting for 65% of the market share (ammonia and methanol synthesis ≈63%; liquid hydrocarbons and higher alcohols synthesis ≈2%) and the refining sector, which accounts for 30% of the market share (hydro treating and hydro cracking processes for obtaining high-grade petrochemical products). The other present uses, with ≈5% of the total consumption, include the food industry (sorbitol and fat processing), the metallurgical industry (direct reduction of iron ore), the semiconductor industry and so on. Post covid-19 lockdown, there will be more demand and investment for the hydrogen economy, especially in transport and industrial sectors as source fuel. Covid-19 pandemic has automatically reset world energy consumption toward the hydrogen economy. Global environment will sustain the natural balance of earth for a healthy and clean atmosphere as experienced during the covid-19 lock down with the hydrogen economy.

VI. THE ECONOMIC AND ENVIRONMENT IMPORTANCE OF HYDROGEN AS A VIABLE FUEL OPTION POST COVID-19 PANDEMIC

Australia, Germany Norway Denmark, United States, Canada, South Korea and Japan have made massive investment toward hydrogen economy, more seriously energy and environmentally concern countries are also actively developing and investing their own (Abe et al., 2019) because the future of world energy consumption is toward hydrogen economy .In order for hydrogen to be considered an economically viable fuel option it must be produced and delivered at a stable price that is competitive with the current price of refine petroleum (gasoline /diesel). Furthermore, the cost of hydrogen economy infrastructure development must be considered, the availability and accessibility of hydrogen must be realized through production and distribution capacity. Some existing pipelines could even be modified support hydrogen economy for distribution. However a long-distance distribution network may not required as hydrogen can be produced regionally where it is needed. One major benefit of hydrogen is that it can be produced from a variety of primary sources and different production process as earlier discussed; therefore accessibility of hydrogen could be almost anywhere in the world. Another benefit of hydrogen over other fuel option is that after combustion/reaction product is water vapour there is no carbon foot print or green house gases. The world will be in its natural state as experienced during covid-19 locked down. Using hydrogen as feasible fuel option will not change our transport system as hydrogen can be used as fuel directly in an internal combustion engines not much different from engines used with gasoline (Balat, 2005).

As viable fuel option for industrial and transport sector, hydrogen has peculiar properties which include rapid burning speed which enhances

performance of engines, high octane number with non toxicity and ozone forming potential. A hydrogen engine is easy to start in extreme cold weather condition because its remain in gaseous state until it reaches a low temperature such as 20K (Ma et al., 2003). Although engine combustion products of hydrogen are clean; consisting of water and little amount of nitrogen oxides (NO_X), since there is little or no presence of volatile organic compounds a steady state of natural balance will always be achieved where relative low ozone exist naturally in the troposphere of the Earth. Production hydrogen from electrolysis from splitting of water can result to elevated oxygen level which may enhance good breathing for land and aquatic life. With hydrogen as fuel option the earth will always be its fresh natural state and human health will not threaten. Life span of people where hydrogen economy is entrenched is likely to increase. The planet can become hopeful of climate neutrality in the years ahead with hydrogen economy. A hydrogen economy has long terms goal of many nations, can potentially confer and be a solution to energy security, along with financial, environmental and health benefits to the world.

VII. CONCLUSION

No doubt Post covid-19 pandemic will be a time for global energy shift toward hydrogen economy. Hydrogen economy will make the world better place for improved public health living, the environment will be devoid anthropogenic pollutions from fossil fuel and there will be sustainable earth balance. Hydrogen economy comes with increase in oxygen level in atmosphere. Life span of living matter may likely to improve. Hydrogen economy will lead to decarbonization of the atmosphere as there are no carbon footprint in the hydrogen engine emissions. With hydrogen economy there is no political power tussle and economic unrest as hydrogen fuel could be produce anywhere in the world. Hydrogen economy has the potential of more jobs creation and other economic benefits. It can result to stable, inexhaustible energy supply .Electricity becomes cheap and energy is readily accessible. The world will be a better place and relatively at peace. Hydrogen economy is the only energy resources that can meet world energy needs, its emission goal and find appropriate solution for region of the world. Hydrogen economy is a more reliable and resilient energy system.

REFERENCE

1. Prince-Richard S, Whale M, and Djilali N (20 05). A Techno - economic Analysis of Decentralized Electrolytic Hydrogen Production for Fuel Cell Vehicles. International Journal of Hydrogen Energy; 30(11):1159-1179.
2. Abe JI, Popoola API, Ajenifuja E, Popoola OM. Hydrogen Energy, Economy And Storage: Review And Recommendation. International Journal of Hydrogen Energy 2019.44:44:1507 2-86.
3. Balat Mustafa. Current alternatives engines fuels. Energy sources part a 2005; 27:569.
4. Ma J, Su Y, Zhou Y, Zhang Z, Simulation and Prediction of the Performance of Vehicle Hydrdrogen engines. International Journal of Hydrrogen Engines.2003;28:127.
5. United States Department of Energy: National Hydrogen Energy Roadmap, Production, Delivery, Storage, Conversion, Applications, Public Education and Outreach (2002). Washington DC.
6. Charvin P, Stephane A, Florent L, Gilles F. Analysis of solar chemical processes for hydrogen production from water splitting thermochemical cycles. Energy Conver Manage 2008;49:1547.
7. Sigurvinsson J, Mansilla C, Arnason B, Bontemps A, Marechal A, Sigfusson TI, et al. Heat transfer problems for the production of hydrogen from geothermal energy. Energy Conver Manage 2006; 47:3543.
8. Press, Roman J.; Santhanam, K. S. V.; Miri, Massoud J.; Bailey, Alla V.; Takacs, Gerald A. (2008). Introduction to hydrogen Technology. John Wiley & Sons. ISBN 978-0-471-77985-8.
9. Häussinger, Peter; Lohmüller, Reiner; Watson, Allan M. (2011). Hydrogen: Properties and Occurrence. Ullmann's Encyclopedia of Industrial Chemistry doi:10.1002/14356007.a13_2 97.pub2. ISBN 978-3-527-30673-2.
10. Norbeck JM, Barth MJ, Farrell JA, Heffel JM. Development and evaluation of a hydrogen

fuel power plant for hybrid electric vehicles–phase 2. Final report to the South Coast Air Quality Management District under contract 95073, project 7; December, 1997.
11. Balat M. Hydrogen in Fueled Systems and the Significance of Hydrogen in Vehicular Transportation. Energy Sources Part B 2007; 2:49.
12. Demirbas A. Fuel properties of hydrogen, liquefied petroleum gas (LPG), and compressed natural gas (CNG) for transportation. Energy Sources Part A 2002; 24:601.
13. Funk J. Thermochemical hydrogen production: past and present. Int J Hydrogen Energy 2001; 26:185.
14. Kaneko H, Gokon N, Hasegawa N, Tamaura Y. Solar thermochemical process for hydrogen production using ferrites. Energy 2005;30:21 71.
15. Plass Jr., J. H., F. Barbõ r, H. P. Miller, and T. N. VeziroÆglu. 1990. Economics of hydrogen as a fuel for surface transportation. Int. J. Hydrogen Energy 15:663–668.
16. Berry, G. D., A. D. Pasternak, G. D. Rambach, J. R. Smith, and R. N. Schock. 1996. Hydrogen as a future transportation fuel. Energy 21:289 –303.
17. Bockris JO and Veziroglu N Estimates of the price of hydrogen as a medium for wind and solar sources. Int J Hydrogen Energy 2007; 32: 1605.
18. Granovskii M, Dincer I, Rosen MA. Exergetic life cycle assessment of hydrogen. production from renewables. J Power Sources 2007; 167:461 .
19. Tarnay DS. Hydrogen production at hydropower plants. Int J Hydrogen Energy 1985; 10:577.
20. Utgikar V, Thiesen T. Life cycle assessment of high temperature electrolysis for hydrogen production via nuclear energy. Int J Hydrogen Energy 2006; 31:939.
21. Acar, C., & Dincer, I. (2014). Comparative assessment of hydrogen production methods from renewable and non-renewable sources. International Journal of Hydrogen Energy, 39(1), 1–12. https://doi.org/10.1016/j.ijhydene.2013.10.060
22. Acar, C., and Dincer, I. (2017). Energy and exergy analyses of a novel photoelectrochemical hydrogen production system. International Journal of Hydrogen Energy, 42(52), 30550–30558. https://doi.org/10.1016/j.ijhydene.2017.10.008.
23. Benefits of the Hydrogen Economy—Hydrogen Energy Center. (n.d.). Retrieved January 11,2020, from https://www.Hydrogenenergycenter.org/benefits-of-the-hydrogen-economy.
24. Deiana, P., Pettinau, A., and Tola, V. (2007). Hydrogen production from coal gasification in updraft gasifier with syngas treatment line. 1.
25. Dincer, I., and Acar, C. (2014). Review and evaluation of hydrogen production methods for better sustainability. International Journal of Hydrogen Energy, 40(34), 11094–11111. https://doi.org/10.1016/j.ijhydene.2014.12.035
26. How is hydrogen stored ? | Air Liquide Energies. (n.d.). Retrieved January 11, 2020, from https://energies.airliquide.com/resources-planet-hydrogen/how-hydrogen-stored.
27. Hydrogen Production: Thermochemical Water Splitting | Department of Energy. (n.d.). Retrieved January 8, 2020, from https://www.energy.gov/eere/fuelcells/hydrogen-production-thermochemical-water-splitting.
28. Mazloomi, K., and Gomes, C. (2012). Hydrogen as an energy carrier: Prospects and challenges. Renewable and Sustainable Energy Reviews, 16(5), 3024–3033.https://doi.org/10.1016/j.rser.2012.02.028.
29. Momirlan, M., & Veziroglu, T. N. (2005). The properties of hydrogen as fuel tomorrow in a sustainable energy system for a cleaner planet. 30, 795–802. https://doi.org/10.1016/j.ijhydene.2004.10.011.
30. Sharma, S., and Ghoshal, S. K. (2015). Hydrogen the future transportation fuel: From production to applications. Renewable and Sustainable Energy Reviews, 43, 1151–1158. https://doi.org/10.1016/j.rser.2014.11.093
31. Vozniuk, O., Tanchoux, N., Millet, J., Albonetti, S., Renzo, F. Di, & Cavani, F. (2019). Spinel Mixed Oxides for Chemical-Loop Reforming : From Solid State to Potential Application. In Horizons in Sustainable Industrial Chemistry and Catalysis (1st ed., Vol. 178). Elsevier B.V. https://doi.org/10.1016/B978-0-444-64127-4.00014-8.

32. Australian Renewable Energy Agency. Hydrogen Energy 16 December 2019.arena.gov.au/renewable-energy/hydroge/.
33. Gronewold N. Momentum builds for hydrogen fuel in Japan, Australia. 2019. www.scientificamerican.com/article/momentum-build-for--hydrogen-fuel-in-japan-australia.
34. International Energy Agency. World energy outlook 2017. 2017. Available from:https://webstore.iea.org/worldenergy-outlook-2017.
35. Shaikh F, Ji Q, Fan Y. Evaluating China's natural gas supply security based on ecological network analysis. J Clean Prod 2016;139:1196e206.
36. The paris agreement. Available from:https://unfccc.int/process/the-paris-agreement/what-is-the-paris-agreement; 2015.
37. Lin B, Xu M. Regional differences on CO2 emission efficiency in metallurgical industry of China. Energy Pol 2018;120:302e11.
38. Tilt B. China's air pollution crisis: Science and policy perspectives. Environ Sci Pol 2019;92:275e80.
39. Vozniuk, O., Tanchoux, N., Millet, J., Albonetti, S., Renzo, F. Di, & Cavani, F. (2019). Spinel Mixed Oxides for Chemical-Loop Reforming : From Solid State to Potential Application. In Horizons in Sustainable Industrial Chemistry and Catalysis (1st ed., Vol. 178). Elsevier B.V. https://doi.org/10.1016/B978-0-444-64127-4.00014-8..
40. Sharma, S and Ghoshal, S. K. (2015). Hydrogen the future transportation fuel: From production to applications. Renewable and Sustainable Energy Reviews, 43, 1151–1158. https://doi.org/10.1016/j.rser.2014.11.093.
41. Dincer, I., & Acar, C. (2014). Review and evaluation of hydrogen production methods for better sustainability. International Journal of Hydrogen Energy, 40(34), 11094–11111. https://doi.org/10.1016/j.ijhydene.2014.12.035 .
42. Acar, C., and Dincer, I. (2017). Energy and exergy analyses of a novel photoelectrochemical hydrogen production system. International Journal of Hydrogen Energy, 42(52), 30550–3055 8. https://doi.org/10.1016/j.ijhydene.2017.10.008.
43. Mustafa Balat. Potential importance of hydrogen as future solution to environmental and transport problems. International Journal of Hydrogen Energy 33 (2008) 4013–4029.
44. Zanganeh KE, Shafeen A. A novel process integration, optimization and design approach for large-scale implementation of oxy-fired coal power plants with CO2 capture. Int J Greenhouse Gas Cont 2007;1:47.
45. Meher LC, Sagar DV, Naik SN. Technical aspects of biodiesel production by transesterification and a review. Renew Sustain Energy Rev 2006;10:24.
46. Campen A, Mondal K, Wiltowski T. Separation of hydrogen from syngas using a regenerative system. Int J Hydrogen Energy 2008;33:332.
47. Suban M, Tug˘ek J, Uran M. Use of hydrogen in welding engineering in former times and today. J Mater Process Technol 2001;119:193 Source of hydrogen.
48. Mariolakos I, Kranioti A, Markatselis E, Papageorgiou M. Water, mythology and environmental education. Desalination 2007;213:141.
49. Wang J, Tang K, Feng K, Lv W. High Temperature and High Humidity Reduce the Transmission of COVID-19. Available at SSRN 3551767 2020-
50. Chen B, Liang H, Yuan X, Hu Y, Xu M, Zhao Y, et al. Roles of meteorological conditions in COVID-19 transmission on a worldwide scale. medRxiv 2020.
51. Ma Y, Zhao Y, Liu J, He X, Wang B, Fu S, et al. Effects of temperature variation and humidity on the mortality of COVID-19 in Wuhan. medRxiv 2020.
52. Bauwen M, Compernolle S,Stavrakou T,Muller JF, van Gent J, Eskes H, Levelt, R vander A. Veefkind J.P, Veefkind J, Huan Yu, C. Zehner. Impact of coronavirus outbreak in NO2 pollution assessed using TRIPOMI and OMI observations. American Geophysical Union. 2020.
53. Allen JA, Glenn M, Hapugoda P, Stanger R, O'Brien G, Donne SW, 'An investigation of mineral distribution in coking and thermal coal chars as fuels for the direct carbon fuel cell', Fuel, 217 11-20 (2018).

This page is intentionally left blank

Calculating Method of Tool Tilt Angle by Solving of Quadratic Equations in 5-Axis Machining with Flat-End Cutter

Gyong Wal Jang , Nam Chol Yu , Hyon Chol Hwang , Guan Sik Jang & Tae Jin Bang

Kim Chaek University of Technology

ABSTRACT

This paper proposes a method for calculating the tilt angle of the tool and the machining strip width when the tool is inclined to the feed direction. We considered the geometry of the surface and the tool as well as the scallop height to determine the tool tilt angle, thus ensuring the tool to be contacted with the surface at two points. This allows us to calculate the tool tilt angle and the machining strip width by solving quadric equations based on the contact circle. An experiment of machining on the quintic B-spline surface was performed and the results show that the proposed method has considerably higher machining efficiency than the CMM.

Keywords: flat-end cutter; tilt angle; machining strip width; scallop height.

Classification: FOR Code: 861499

Language: English

London Journals Press

LJP Copyright ID: 392964
Print ISSN: 2631-8474
Online ISSN: 2631-8482

London Journal of Engineering Research

Volume 21 | Issue 1 | Compilation 1.0

Calculating Method of Tool Tilt Angle by Solving of Quadratic Equations in 5-Axis Machining with Flat-End Cutter

Gyong Wal Jang[α], Nam Chol Yu[σ], Hyon Chol Hwang[ρ], Guan Sik Jang[ω] & Tae Jin Bang[¥]

ABSTRACT

This paper proposes a method for calculating the tilt angle of the tool and the machining strip width when the tool is inclined to the feed direction. We considered the geometry of the surface and the tool as well as the scallop height to determine the tool tilt angle, thus ensuring the tool to be contacted with the surface at two points. This allows us to calculate the tool tilt angle and the machining strip width by solving quadric equations based on the contact circle. An experiment of machining on the quintic B-spline surface was performed and the results show that the proposed method has considerably higher machining efficiency than the CMM.

Keywords: flat-end cutter; tilt angle; machining strip width; scallop height.

Author α ¥: Robotics Institute, Kim Chaek University of Technology, Pyongyang, DPR Korea.
σ: School of Science and Engineering, Kim Chaek University of Technology, Pyongyang, DPR Korea.
ρ: Control Machine Institute, Academy of state science, Pyongyang, DPR Korea.
ω: Faculty of Mechanical Science and Technology, Kim Chaek University of Technology, Pyongyang, DPR Korea.

I. INTRODUCTION

5-axis machining tools are widely used for sculptured object machining in aircrafts, automobiles, molds, dies, etc. A sculptured surface is often machined with a ball-end cutter in a 3-axis NC machine tool. Traditionally, the ball-end cutter is widely used in sculptured surface machining for the highly flexible controllability. But the process efficiency is low especially for freeform surface machining, which generally needs multiple tool-paths. Some researchers describe that the feasible adjustment of the tool orientation by the two additional degrees of freedom in flat-end or filleted-end cutter 5-axis machining achieves higher efficiency than ball-end cutter 3-axis machining [1].

The main problems in 5-axis tool path generation are feasible tool orientation determination, avoidance of tool collisions, tool path phase, etc., of which the determination of tool orientations is the most important in increasing the machining strip width within a given tolerance. In 5-axis NC machining, flat-end or filleted-end cutters are known to be much more effective than a ball-end cutter with same diameter. Therefore, many methods have been proposed to determine the tool orientation with different types of cutters. To improve the machining efficiency of multi-axis flank milling of freeform surface, Ming Luo et al proposed a novel barrel cutter design method [2].

The simplest Sturz method has been widely used in the commercial CAD/CAM systems such as UGS NX. In the Sturz method, the tool is traditionally inclined for a constant angle that may range from 5 to 15° to the feed direction about the CC point in the plane containing the CC point, the feed direction and the surface normal. If the tilt angle is too high, then lower gains in metal removal rate will occur. Otherwise, if it is too low, then the tool may gouge the designed surface. Therefore, the tilt angle must be chosen carefully so that no rear gauging occurs during the machining. But, it could not be expected that the machining would be efficient because the tilt angle is determined irrespective of the geometry of the tool and the surface in the neighborhood of

London Journal of Engineering Research

the contact point. A searching method in the machining configuration space (C-space) is proposed to find the optimal tool orientation by considering the local gouging, rear gouging and global tool collision in machining. By using the minimum cusp height as the objective function, first determine the locally optimal tool orientation in the C-space to minimize the machined surface error. Considering the adjacent part geometry and the alternative feasible tool orientations in the C-space, tool orientation are then globally optimized and smoothed to minimize the dramatic charge of tool orientation during machining [3]. Tool postures of the flat-end cutter can make a huge difference to both machining strip width and machining efficiency in five-axis end milling. Most of current methods evaluate the machining strip width and implement a tool orientation optimization by finding two intersection points between the effective cutting profile of a flat-end cutter and the offset surface profile which represents machined surface. However, real machining strip width and real residual height should be formed between two adjacent cutter contours. In order to solve the above problems, Baohai Wu et al presented and proved a more suitable method for computing machining strip width [4]. Rao et al. examined the effect of feed on the machined surface for tool orientations using the Principal Axis Method (PAM). In the PAM, the orientation of tool is determined based on the geometric properties of tool and surface at the CC point. The feed direction is selected to be in the direction of minimum curvature calculated at each CC point [5]. The PAM is a special case for the curvature matched machining (CMM). The iterative search for an angle that does not cause gouging used the tilt angle calculated from the maximum curvature as a starting point. Each tool orientation must be incrementally checked for gouging and adjusted until it is gouge-free. It is known that PAM provides lower efficiency than MPM. Lee proposed a non-isoparametric tool path generation method, which feasibly evaluates the machining strip width in flat-end cutter 5-axis surface machining. In this method, the disjointed segments of non-parametric offset path should be connected for smooth tool movements. Furthermore, discontinuities in the surface curvature may also cause lacking smoothness in the trajectory of a tool center or in the curve of cutter contact points on a surface. The fixed tilt angle of tool was used in his experiments [6].

Generation of efficient tool paths is essential for the cost-effective machining of parts with complex free-form surfaces. A new method to generate constant scallop height paths for the efficient five-axis machining of free-form surfaces using flat-end mills is presented. The tool orientations along the tool paths are optimized to maximize material removal and avoid local gouging. The distances between adjacent tool paths are further optimized according to the specified scallop height constraint to maximize machining efficiency. The constant scallop height tool paths are generated successively across the design surface from the immediate previous tool path and its corresponding scallop curve. An offset surface of the three-dimensional design surface based on the spacified scallop height, is used to establish accurately the scallop curve with the constant scallop height [7]. Lo presented a method of tuning adaptively the tilt angle of the flat-end cutter so that the machining strip width can be as large as possible in 5-axis machining with a flat-end cutter. In this method, the cutter paths were scheduled so that the scallop height formed by two adjacent machining paths was constant [8]. Anotaipaiboon et al. presented the concept of an adaptive space-filling curve for tool path planning for five-axis NC machining of sculptured surfaces. Generation of the adaptive space-filling curves requires three steps: grid construction, generation of the adaptive space-filling curve, and tool path correction. The space-filling curves, adapted to the local optimal cutting direction, produce sculptor tool paths. This method is endowed with a new modification of techniques for computing the machining strip width along with a modified formula for the minimum tool inclination angle to avoid gouging [9]. Chiou et al. presented a machining potential field (MPF) method to generate tool paths for multi-axis sculptured surface machining. A machining potential field is constructed by considering both the part geometry and the cutter geometry to represent the machining-oriented information on

the part surface for machining planning. The largest feasible machining strip width and optimal cutting direction at a surface point can be found on the constructed machining potential field. The tool paths can be generated by following the optimal cutting direction. Feasible cutter sizes and cutter orientations can also be determined by using the MPF method [10].

Some researchers proposed a Coordinate Matched Method (CMM) that the effective cutting radius of the tool matches the curvature radius of the section curve on the plane normal to the surface at the CC point for better machining efficiency in 5-axis surface machining. Wang et al. presented a 3D curvature matched machining method and a curvature gouge detection and elimination method for 5-axis surface machining. This method is based on the Eular-Meusnier spheres concept and the geometric model of surface curvature geometry [11]. Shanming Luo et al. proposed the curvature matching method and the minimum distance method to inspect interferences occurring in the five-axis end milling of cycloidal gears [12]. Jensen et al. presented a method for determining the tool orientation based on the CMM in 5-axis finish surface machining. The tool is inclined to the direction corresponding to minimum principle curvature of the designed surface, and the tilt angle is adjusted until the "effective cutting radius" of tool is equal to the radius of maximum curvature of the designed surface at the CC point [13].

Some researchers presented various methods for determining the optimal tool orientation.

Wang et al. presented a 5-axis tool-path generation algorithm for alleviating the abrupt change of tool orientations when the tool orientation was adaptively determined to avoid the local and global gouge [1]. Feng et al. examined the effect of tool tilt angle on the machining strip width in determining the optimal tool orientation and feed direction in 5-axis flat-end milling [14].

On the other hand, Warkentin et al. proposed a Multi-Point Machining (MPM) method for higher effectiveness in 5-axis NC machining. In MPM, there exist more than one-point contact between the desired surface and the cutting tool [15]. Also proposed an efficient algorithm that generate the multi-point positions of tool. Their algorithm was found to be less effective for complex surface machining [15] and [16]. Warkentin et al. compared MPM with the Sturz method and the PAM, and showed that the scallop height generated in 5-axis machining using MPM is much smaller than the others [17]. In MPM, the tool is positioned such that there are two CC points. This method is mathematically complicated because it needs search of specific areas for potential candidates for the second cutter point for each tool position after the first CC point is predetermined. The tool is forced to maintain contact at the first CC point. It is then rotated about two independent axes until an optimal position is achieved that minimizes the distance between the tool and the second CC point. Among two independent axes, one is the feed direction and the other is a vector normal to the plane that includes the feed direction and perpendicular to the surface. This method is still much complicated than other methods and would have a limited use in industry due to the complexities of the algorithm.

Together with the tool orientation, the tool path phase has a large influence on the machining efficiency. The simplest approach is the iso-parametric method which use the curves of constant parameter. For the iso-parameter machining, if the feed direction is set along the u parameter, the tool paths are generated by incrementing the v parameter. Here, the path interval must be set carefully because the scallop height between the tool paths could not be constant. Another approach for the tool path generation is to use intersection curves of parametric surface and a series of vertical planes. For this iso-plane machining, the path interval or the distance between the vertical planes is also determined based on the scallop height limitation. For both iso-parameter and iso-plane approaches, the scallop height could not be maintained to be constant. The iso-scallop height approach was proposed to overcome this drawback.

The Point-In-Convex-Hull-Control (PICHC) method is presented for the calculation of the optimum tool orientation during the 5-axis simultaneous CNC machining of sculptured surfaces. More specifically, this novel exact multi -point algorithm minimizes the clearance and/or overclosure of the contact surface between the tool and the work piece and maximizes the material removal rate [18]. Convex edge surfaces are always encountered in industry, such as the leading and trailing edges of turbine blades. Concave cutter can be used to flank machine such surfaces. The fundamental theory is given by investigating the conjugation between a concave cutter and a cylindrical surface. By analyzing the projection of the grazing curve in the cross-section plane, it finds that convex edge surface with various cross-section radiuses can be machined with a concave cutter by adjusting the cutter orientation [19]. Machchhara et al. presents an algebraic based approach and a computational framework for the simulation of multi-axis CNC machining of general freeform tools. The boundary of the swept volume of the tool is precisely modeled by a system of algebraic constraints, using B-spline basis functions [20]. The Drop and Spin Method (DSM), a multipoint tool positioning technique for five-axis machining of corners formed by the intersection of two bi-quadratic Bazier surfaces with a toroidal end mill is presented by Kumar Sharma et al. In the DSM the tool is dropped onto one of the surfaces to identify the first point of contact. The second point of contact is determined on the second surface. These two points of contact ensure that the toroidal tool can be positioned in the closest possible proximity to the two surfaces along the common edge [21]. To solve the problem of the poor machining quality of the leading and trailing edge surface of the aircraft engine blade, a tool path generation method based on smooth machine rotary angle and tilt angle in five-axis surface machining with torus cutters was proposed by Zhang et al. In terms of a specified type of five-axis machine tool, a relationship equation between design variables of tool position and machine rotary angles was firstly derived. A new tool orientation smoothing approach was then put forward. On this foundation, a tool path generation method based on a smooth machine rotary angle and tilt angle was presented [22].

As mentioned above, a flat-end cutter is still widely used in industry with a fillet-end cutter. Many previous studies considered only a single CC point in flat-end cutter 5-axis machining when determining the tool orientation. The machining efficiency could be increased with multi contact points as MPM. In this paper, we propose a simple method for calculating the tool tilt angle and the machining strip width when the tool is inclined to the feed direction in order to maximize the machining strip width in flat-end cutter five-axis surface machining. And we verify the effectiveness through the machining experiments.

This paper is divided into five sections. The section 1 gives a brief overview of various concepts and notations in 5-axis machining and then, Section 2 gives explanations of the method for calculation of tool tilt angle and machining strip width based on the contact circle and the scallop height. In Section 3, the machining experiments are shown based on the proposed method.

II. THEORETICAL BACKGROUND

Fig.1 shows a rotated flat-end cutter of radius R at a **CC** point and the associated coordinate systems in 5-axis surface machining with a flat-end cutter. A local coordinate system is established at the **CC** point on the design surface. The **CC** point is the origin of this local coordinate system. In the local coordinate system, **n** is the unit vector in the surface normal direction and **f** is the unit vector in the feed direction and **k** = **n** x **f**.

In 5-axis machining, the tool orientation is defined by 2 rotation angles. The tool is first rotated about **t** for an tilt angle ϕ and then about **n** for a tilt angle β. Tool coordinate system (TCS) is established by the center of the bottom tool circle (BTC) of the flat-end cutter as the origin and tool axis as $\mathbf{t}_{axis}$.

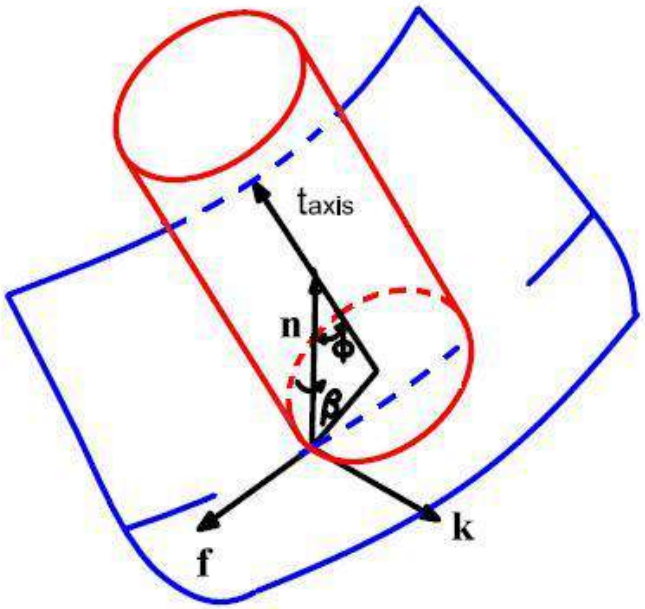

Fig. 1: Machining with flat-end cutter

It was known that the machining efficiency is good when the feed direction is chosen as the maximum curvature direction [7]. However, they assume that the feed direction is arbitrarily predefined.

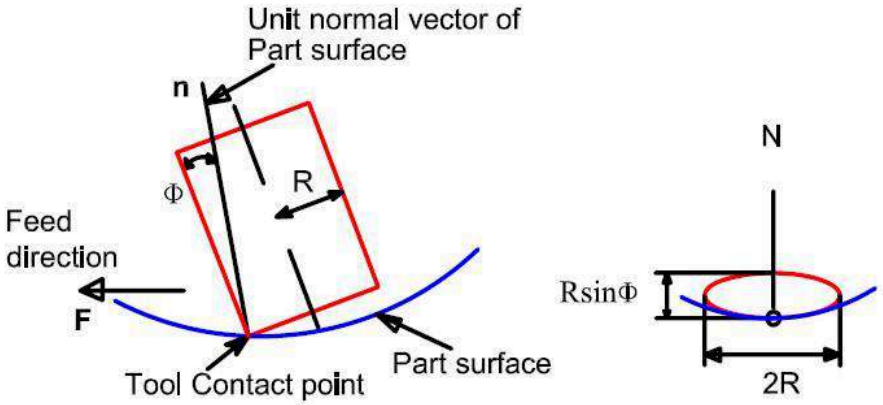

Fig. 2: Cutting ellipse

When the contact point between the tool and the designed surface is only one, the orthogonal projection of the bottom edge of tool on k-n plane is called the cutting ellipse and the curvature radius of this ellipse at CC point is called the cutting radius as shown in Fig. 2. In Fig. 3, the tool axis is inclined for an angle ϕ to the feed direction and contacts with the part surface at CC point. The plane formed by the tool axis and the feed direction is called the tool axis plane.

A unit vector $\boldsymbol{e}$ is defined as:

$$\mathbf{e} = \mathbf{n} \times (\mathbf{n} \times \mathbf{f})$$

Then the unit vector for the tool axis is

$$\mathbf{t}_{axis} = \cos(\varphi)\mathbf{n} + \sin(\varphi)\mathbf{e} \quad (1)$$

And the tool position $\mathbf{t}_{pos}$ can be expressed as

$$\mathbf{t}_{pos} = \mathbf{cc} + R\sin(\varphi)\mathbf{n} - R\cos(\varphi)\mathbf{e} \quad (2)$$

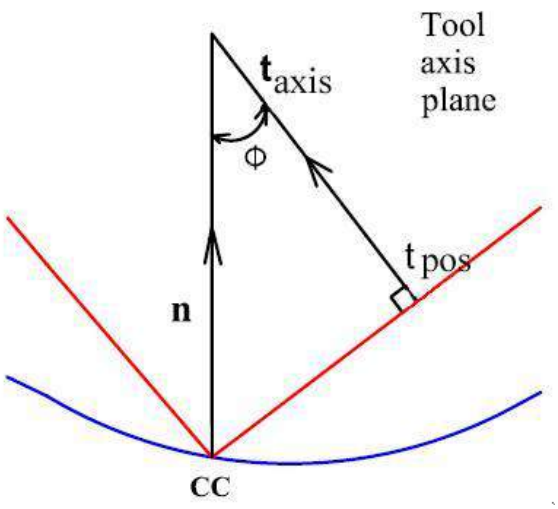

Fig. 3: Situation of tool in the tool axis plane

Suppose that the local normal curvature of the machined surface at the CC point perpendicular to the feed direction is κ. Then, the cutting radius is $\frac{\sin(\phi)}{R}$ when the tool tilt angle is ϕ. Thus,

$$\kappa = \frac{\sin(\phi)}{R}$$

As a result, the tool tilt angle can be determined by using the local normal curvature of the surface as follows:

$$\phi = \arcsin(\kappa \cdot R) \qquad (3)$$

Calculation of a machining strip width by one contact point method was carefully explained in [6].

III. METHOD

3.1: Determination of a tool tilt angle based on the contact circle

The scallop height forms the residual after machining and is removed during the fine finish process. Previously, the machining strip width was evaluated based on this scallop height. The scallop height is an important factor that effects on the machining strip width. The machining strip was defined as the machined region that lies within the required scallop height limits, where the scallop height was not greater than the tolerance. From the viewpoint of the permissible tolerance, this means that the scallop height is not greater than the permissible tolerance at all points within the machining strip, and never means that the tool must be surely contacted with the surface within the machining strip.

Now, we consider the tool orientation in which the tool contacted with the machined surface at 2 points and with the offset surface at one point as shown in Fig. 4. The tool is assumed to be inclined to a predetermined direction. In Fig. 4, the point $\mathbf{cc}_0$ is generated by translating the reference contact point cc with the given tolerance δ to the direction perpendicular to the surface. The tool is inclined to the machining direction about the axis $\mathbf{k}_1$, which passes through the point cc_0 and perpendicular to the machining direction.

The intersection curve of the **t-n** plane and the machined surface can be approximated by a contact circle with a radius equal to the major radius of the effective cutting ellipse. Here, the bottom circle of the inclined tool intersects at two points with the contact circle when the tool is inclined in the feed direction as shown in Fig. 4. Fig. 4 also shows the situation of the cutting ellipses in the case of one contact point. As shown in Fig. 4, we can expect that the machining strip width W would be much greater than the

machining strip width W_{FAM} at only one contact point.

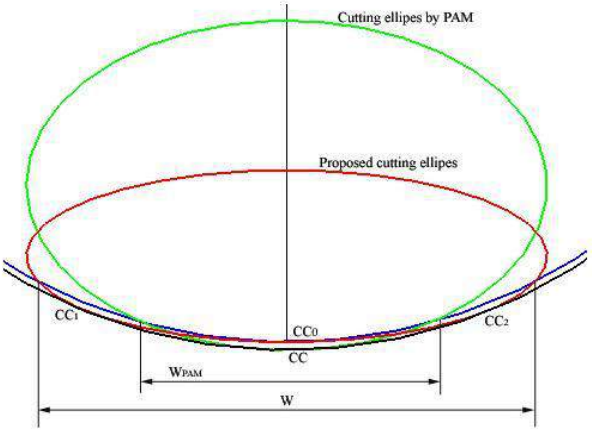

Fig. 4: Arrangement of cutting ellipses at one point of contact and two points of contact

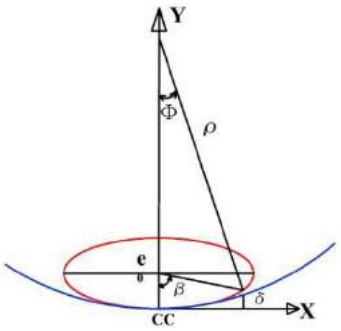

Fig. 5: Relation between the contact circle and the cutting ellipse at a contact point

First, we consider the case in which the cutting ellipse contacts with the contact circle at the cc point. In Fig. 5, **ρ** is the radius of the contact circle. As shown in Fig. 5, the points on the circumstance of the contact circle in the coordinate system with the cc point as the origin is described as follows:

$$\begin{cases} x = \rho \sin\varphi \\ y = \rho - \rho\cos\varphi \end{cases}$$

Then

$$\sin\varphi = \frac{x}{\rho}, \cos\varphi = \frac{\rho - y}{\rho}$$

Therefore,

$$\frac{x^2}{\rho^2} + \frac{(\rho - y)^2}{\rho^2} = 1$$

$$x^2 = 2\rho \cdot y - y^2 \qquad (4)$$

Fig. 6 shows the situation of the cutting ellipses in the case of two contact points. Let's consider the points on the circumstance of the cutting ellipse, which are the points on the bottom edge of the tool.

The tool is inclined about $\mathbf{k}_1$ until the tool contacts with the contact circle at two points.

When the tool is inclined as long as ϕ in the feed direction, the cutting ellipse has the major radius a=R and the minor radius b=$R\sin\phi$. Then, the center of the ellipse is represented as:

$$\begin{cases} x = 0 \\ y = \delta + R\sin\phi \end{cases}$$

The points on the circumstance of the ellipse are represented as:

$$\begin{cases} x = a\cos\beta = R\cos\beta \\ y = \delta + R\sin\phi - R\sin\phi\sin\beta \end{cases}$$

Thus,

Thus,

$$\cos\beta = \frac{x}{R},\ \sin\beta = \frac{\delta + R\sin\phi - y}{R\sin\phi} \quad \frac{x^2}{R^2} + \frac{(\delta + R\sin\phi - \mathrm{y})^2}{R^2\sin^2\phi} = 1 \tag{5}$$

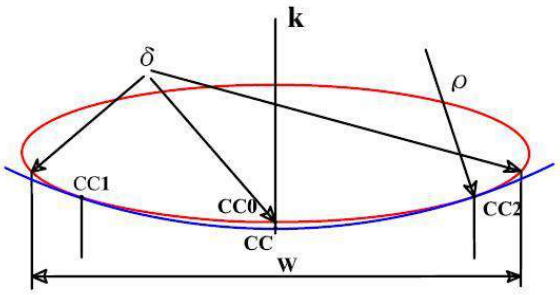

Fig. 6: Relation between the contact circle and the effective cutting ellipse at two contact points.

From Eqs. (4) and (5), we can obtain the position (x(ϕ), y(ϕ)) of the point at which the cutting ellipse and the contact circle are contacted.

$$2\rho\cdot y - y^2 = R^2 - \frac{1}{\sin^2\phi}(\delta + R\sin\phi - \mathrm{y})^2 \tag{6}$$

$$(1-\sin^2\phi)y^2 + 2(\rho\sin^2\phi - \delta - R\sin\phi)y + \delta^2 + 2\delta R\sin\phi - R^2\sin^2\phi = 0$$

Now, the determinant for extreme value of **y** is as following.

$$D = (\rho\sin^2\phi - \delta - R\sin\phi)^2 - (1-\sin^2\phi)(\delta^2 + 2\delta R\sin\phi - R^2\sin^2\phi) = 0$$

Let's $\sin\phi$ be *X*. Then the above equation can be rewritten as:

$$(\rho X^2 - \delta - RX)^2 - (1-X^2)(\delta^2 + 2\delta RX - R^2X^2) = 0 \quad (\rho^2 - R^2)X^4 + (-2\rho\delta R + 2\delta R)\mathrm{X}^3 + (-2\rho\delta + 2R^2 + \delta^2)X^2 = 0$$

$$(\rho^2 - R^2)X^2 - 2\delta R(\rho - 1)\mathrm{X} + (2R^2 - 2\rho\delta + \delta^2) = 0$$

where the solution $X = \sin\phi = 0$ is ignored.

$$X_{1,2} = \frac{\delta R(\rho-1) \pm \sqrt{(\delta R(\rho-1))^2 - (\rho^2 - R^2)(2R^2 - 2\rho\delta + \delta^2)}}{(\rho^2 - R^2)}$$

Therefore, the tilt angle of the tool is calculated as:

$$\phi_{1,2} = \arcsin X_{1,2} \tag{7}$$

From the two solutions, the minimum value is only selected because the smaller the tilt angle, the larger the machining strip width.

The machining strip width can be calculated from the fact that the difference between the value *y* of equation for the contact circle and the value *y* of the cutting ellipse is equal to δ. As a result, instead of Eq. (6), we can get the following equation.

$$2\rho\cdot(y+\delta) - (y+\delta)^2 = R^2 - \frac{1}{\sin^2\phi}(\delta + R\sin\phi - y)^2 \tag{8}$$

$$2\rho\cdot(y+\delta)\sin^2\phi-(y+\delta)^2\sin^2\phi=R^2\sin^2\phi-(\delta-y)^2-2(\delta-y)R\sin\phi-R^2\sin^2\phi^2$$

$$(1-\sin^2\phi)y^2+2(\rho\sin^2\phi-\delta\sin\phi-R\sin\phi)y+$$
$$2\rho\,\delta\sin^2\phi+\delta^2+2\delta\,R\sin\phi-R^2\sin^2\phi-\delta^2\sin^2\phi=0$$

From Eq. (8), two values $y_{1,2}$ can be calculated. From the positive values, we select the greater value, and twice that value must be not greater than 2*R*. Then, the machining strip width *W* is calculated as:

$$W=2y \tag{9}$$

Now, the tool tilt angle and the machining strip width along with it can be easily calculated by using analytic methods.

In this way, we determined the tool orientation where the machining strip width could be increased as much as possible when the tool was inclined in the predefined direction, thus establishing the calculating method for the machining strip width.

If κ_1 and κ_2 are the principal curvature of the designed surface at the reference contact point **cc**, ρ becomes the maximum principal curvature radius corresponding to κ_1 when the predetermined feed direction is selected as the minimum principal curvature direction. Then the tool tilt angle and the machining strip width can be also calculated by Eqs. (7), (8) and (9).

Let the angle between the feed direction and the direction of the minimum curvature be denoted as θ, then the machining strip width is described as:

$$W1 = W\cdot\cos(\theta) \tag{10}$$

When θ = 0°, i.e. the machining direction coincides with the direction of the minimum curvature, then the machining strip width is maximum, while when θ = 90°, it is minimum.

Feng et al. [10] studied the influence of the tilt angle on the machining strip width and showed that the direction of minimum curvature is not always the best feed direction for machining all the area of the surface. However, that is still a relatively good direction. If the tilt angle is not so large, the machining strip width in the feed direction can be approximately evaluated by Eq. (9).

Also, based on the reference contact point CC and the tool tilt angle, we can generate the CL data by using Eqs. (1) and (2).

3.2: Tool path search

In 5-axis surface machining, the primary tool path usually starts with the boundary curve of the surface. After determining the primary tool path, the adjacent paths must be determined sequentially.

Lee studied carefully the methods to avoid the tool gouge and obtain the adjacent contact points in 5-axis machining with a flat-end cutter [6].

When the machining strip width, W_o, is determined at the current reference contact point $S(u_o, v_o)$ and is assumed to be the distance between the primary and the adjacent tool paths, the adjacent contact point can be calculated from Eq. (11).

$$\frac{\partial \mathbf{S}}{\partial u}\Delta u+\frac{\partial \mathbf{S}}{\partial v}\Delta v=W_0\mathbf{k} \tag{11}$$

When Δu and Δv – the increment values of parameters *u* and *v*, respectively – are calculated from Eq. (11), the parameters of the reference contact point of the adjacent path are as:

$$u=u_0+\Delta u,\qquad v=v_0+\Delta v$$

However, this point $S(u_o+\Delta u, v_o+\Delta v)$ cannot always be the correct adjacent reference contact point because of the assumption that the machining strip width W_o is the distance between the primary and the adjacent standard contact points.

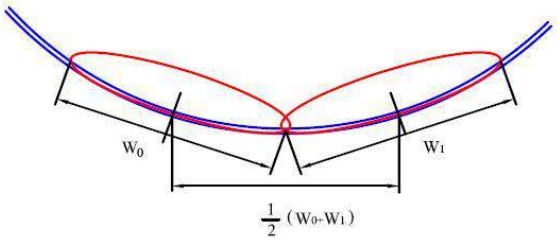

Fig. 7: Search scheme of the adjacent reference contact point

Therefore, regarding $S(u_0+\Delta u,\ v_0+\Delta v)$ as a reference contact point, the machining strip width must be calculated again. In this case, the candidate feed direction is the straight line that connects the two predetermined adjacent reference contact points. And the final parameters of reference contact points of the adjacent tool path are determined by recalculating Δu and Δv based on the following equation:

$$\frac{\partial \mathbf{S}}{\partial u}\Delta u+\frac{\partial \mathbf{S}}{\partial v}\Delta v=\frac{1}{2}(W_0+W_1)\mathbf{k} \tag{12}$$

The local and global gouges in 5-axis machining are solved by the methods proposed by **Lee.** (1998). And the tool tilt angle and tilt angle are adjusted at cc_0.

IV. RESULT AND DISCUSSION

The surface to be machined is a quintic B-spline surface with 36 control points and the CNC machine tool is a dual tool head rotation type(Fig 6). This surface is thought to be such complicated that the efficiency of the proposed method could be verified and concave. The details of values of the control points of the surface are listed in Table. 1.

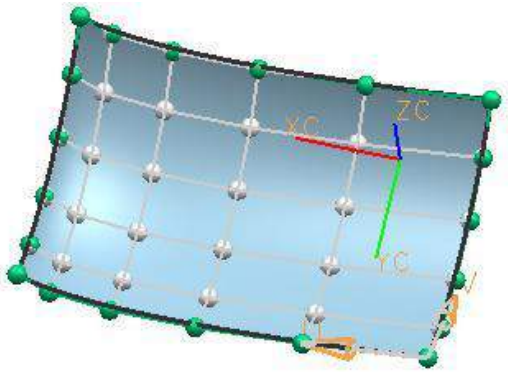

Fig. 8: B-spline surface and control points

The surface is included in the cubic of 187 × 124 × 53(mm) and the minimum curvature radius is 28.25mm. The flat-end cutter with R = 30mm was selected for surface machining.

The allowance for finishing was 0.5mm and the tolerance was 0.03mm. The tool path was generated along with the iso-parametric curves (v-parameter). The tool path was generated in Zig mode for the observation to the tool paths. Fig. 9 shows the situation of the tool path for machining. The CMM required 29 segments of tool path, while the proposed method required 21. As a result, the machining period is 28persents reduced for machining with the same tolerance.

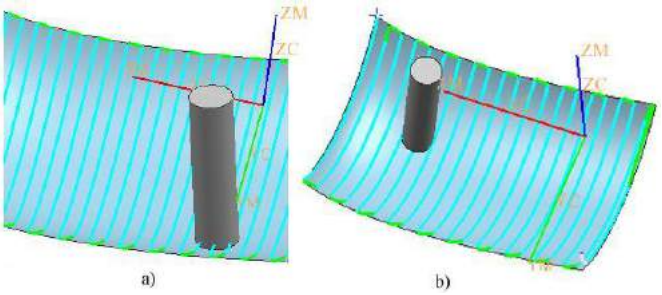

Fig. 9: Tool paths for 5-axis machining by the CMM (a) and the proposed method (b)

Fig. 10 shows the surface deviation produced when machining the sample surface with the CMM and the proposed method. The proposed method can considerably reduce the finishing time because the distributions of residuals are sparse.

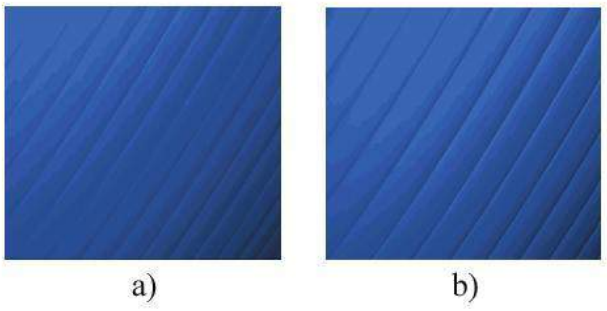

Fig. 10: Surface deviation produced when machining bi-quantic B-spline surface in CMM (a) and the proposed method (b)

Table 1: The control points of sample surface

row		Column1	Column2	Column3	Column4	Column5	Column6
Row1	X	-33.153	24.843	74.154	113.219	140.483	154.39
	Y	88.38	88.38	88.38	88.38	88.38	88.38
	z	0	-15.284	-22.927	-22.927	-15.284	0
Row2	X	-33.153	24.844	74.154	113.219	140.484	154.39
	Y	67.235	67.235	67.235	67.235	67.235	67.235
	z	-19..12	-34.405	-42.047	-42.047	-34.405	-19..12
Row3	X	-33.153	24.843	74.154	113.219	140.484	154.39
	Y	40.568	40.568	40.568	40.568	40.568	40.568
	z	-28.68	-43.965	-51.607	-51.607	-43.965	-28.68
Row4	X	-33.153	24.844	74.154	113.219	140.484	154.39

	Y	12.061	12.061	12.061	12.061	12.061	12.061
	z	-28.68	-43.965	-51.607	-51.607	-43.965	-28.68
Row5	X	-33.153	24.844	74.154	113.219	140.484	154.39
	Y	-14.606	-14.606	-14.606	-14.606	-14.606	-14.606
	z	-19.12	-34.405	-42.047	-42.047	-34.405	-19.12
Row6	X	-33.153	24.843	74.154	113.219	140.484	154.39
	Y	-35.751	-35.751	-35.751	-35.751	-35.751	-35.751
	z	0	-15.284	-22.927	-22.927	-15.284	0

The proposed method is expected to improve concave surface machining. But for the convex surface, the machining efficiency is lowered due to the reduced machining strip width. In this case, one contact point method can be used as in [6].

V. CONCLUSIONS

This paper proposed a method to calculate the tool tilt angle and the machining strip width based on the predefined scallop height in machining where the tool contacts with the surface at two points.

First, we considered the geometry property of the surface and the tool as well as the scallop height, thus considering the tool to be contacted with the surface and the tool. Second, we also calculated the tool tilt angle and the machining strip width by so1ving quadric equations based on the contact circle. Third, we experimented the machine of proposed method and CMM on the biquantic B-spline surface and ensured machining efficiency. In the proposed method, the tool tilt angle and the machining strip width could be analytically calculated by so1ving a quadric equation based on the contact circle. The example have shown that the machining time can be considerably saved and the productivity increased by using the proposed method compared with the CMM.

-Ethical Approval
-Consent to Participate
-Consent to Publish
-Authors Contributions
-Funding
-Competing Interests
-Availability of data and materials

REFERENCES

1. Nan. Wang., Kai. Tang. (2008). Five-axis tool path generation for a flat-end tool based on iso-conic partitioning. Computer-Aided Design, vol. 40, no 12, p.1067-1079, DOI: 10. 1016/ j.cad.09.005.
2. Ming Luo, Dongqing Yan, Baohai Wu & Dinghua Zhang. (2016). Barrel cutter design and toolpath planning for high-efficiency machining of freeform surface. The International Journal of Advanced Manufacturing Technology volume, vol. 85, no.11, p. 2495-2503, DOI :10.1007/s00170 -015-8113-z
3. Jun CS, Cha K, Lee YS. (2003) Optimizing tool orientation for 5-axis machining by configuration-space search method. Computer Aided Design, vol. 35, p.549-566, DOI:10.1016/S00 10-4485(02)00077-3.
4. Baohai Wu, Mancang Liang, Ying Zhang, Ming Luo & Kai Tang. (2018). Optimization of machining strip width using effective cutting shape of flat-end cutter for five-axis free-form surface machining. The Inter- national Journal of Advanced Manufacturing Technology, vol. 94, no. 1, p.2623-2633, DOI:10.1007/s00 170-017- 0953-2.
5. Rao. N., Ismail. F, Bedi. S. (1997). Tool Path planning for five-axis machining using the principal axis method. International Journal of Machine Tools & Manufacture, vol. 37, no.

7, p. 1025-40, DOI:10.1016/s0890-6955 (96) 00046-6.
6. Lee .Y. S. (1998). Non-isoparametric tool path planning by machining strip evaluation for 5-axis sculptured surface machining. Computer-Aided Design, vol. 30, no. 7, p. 559-570,DOI:10.1016/s0010-4485(98)00082 2-7.
7. H.Li, H.Y.Feng. (2004). Efficient five axis machining of free-form surfaces with constant scallop height tool paths. Int J Prod Res, vol. 42, p. 2403-2417, DOI:10.1080/ 00207540310001652905
8. Lo. C-C. (1999). Efficient cutter-path planning for five-axis surface machining with a flat-end cutter. Computer-Aided Design, vol. 31, no. 9, p. 557-566, DOI:10.1016/s0167-4485 (99)00052-4
9. Anotaipaiboon W, Makhanov SS. (2005). Tool path generation for five-axis NC machining using adaptive space-filling curves. Int J Prod Res, vol. 43, p. 1643-1665, DOI:10.1080/00207540412331322948.
10. Chiou CJ, Lee YS. (2002). A machining potential field approach to tool path generation for multi-axis sculptured surface machining. Computer Aided Design, vol. 34,no.9, p. 357-371, DOI:10.1016/S0010-44 85(01)00102-6.
11. Wang. Y J, Dong. Z, Vickers. G W. (2007). A 3D curvature gouge detection and elimination method for 5-axis CNC milling of curved surfaces, Int. J. Adv. Manuf. Technol., vol. 33, p.368-378, DOI 10.1007/s00170-006-08 25-7.
12. Shanming Luo, Longxing Liao, Jian Wang, Yin Wang & Jixiang Yi. (2017). Study on inspection and avoidance of interferences in five-axis end milling of cycloidal gears.The International Journal of Advanced Manufacturing Technology, vol. 91, no. 1, p.3307-3314, DOI:10.1007/s00170-017-0002-1.
13. Jensen. C.G., Red. W.E., Pi. J. (2002). Tool selection for five-axis curvature matched machining. Computer-Aided Design, vol. 34, no. 3, p. 251-256, DOI:10.1016/s0010-4485 (01)00086-0.
14. Fard. M.J.Barakchi., Feng. H. –Y. (2009). Effect of tool tilt angle on machining strip width in five-axis flat-end milling of free-form surface. The international journal of Advanced Manufacturing Technology,vol. 44, p. 211-222, DOI: 10.1007/s00170-008-1828-3.
15. Warkentin. A., Ismail. F., Bedi.S. (1998). Intersection approach to multi-point machining of sculptured surface. Computer- Aided Design, vol. 15, p. 567-584, DOI: 10.1016/s01-67-8396(97)00039-3.
16. Warkentin. A., Ismail. F., Bedi. S. (2000). Multi-point tool positioning strategy for 5-axis machining of sculptured surfaces. Computer Aided Geometric Design, vol. 17, p. 83–100, DOI:10.1016/s0167-8396(99)00040-0.
17. Warkentin. A., Ismail. F., Bedi. S. (2000). Comparison between multi-point and other 5-axis tool positioning strategies. International Journal of Machine Tools & Manufacture, vol. 40, p. 185-208, DOI:10.1016/s08 90-6955(99)00058-9.
18. Andreas Marios Tsainis, George Papazafeiropoulos & Constantinos Stergiou. (2019). A novel convex hull method for optimum multi-point 5-axis tool positioning for machining of complex sculptured surfaces. The International Journal of Advanced Manufacturing Technology, vol. 103,no. 5,p.4369-4383, DOI :10.1007/ s00170-019-03833-9.
19. He Ying, Chen Zhitong & Xu Rufeng. (2016). Research on five-axis flank milling of convex edge surface with a concave cutter. The International Journal of Advanced Manufacturing Technology, vol. 86, no. 2, p.2401-24 09, DOI :10.1007/s00170-016- 8371- 4.
20. Jinesh Machchhara, Denys Plakhotnikb, Gershon Elbera. (2017). Precise algebraic-based swept volumes for arbitrary free-form shaped tools towards multi-axis CNC machining verification. Computer Adied Design, vol. 90, no. 9, p. 48-58, DOI:10.1016/j.cad.2017 .05.015.
21. Sandeep Kumar Sharma, Ravinder Kumar Duvedi, Sanjeev Bedi, Stephen Mann. (2019). A multipoint tool positioning method for five-axis machining in the region of two intersecting tensor product Bazier surfaces. International Journal of Machine Tools and

Manufacture, vol. 142, no. 7, p. 42-53, DOI: 10.1007/s00170-016-8371-4.
22. Yu Zhang, Rufeng Xu, Xun Li, Xiang Cheng, Guangming Zheng & Jianbing Meng. (2020). A tool path generation method based on smooth machine rotary angle and tilt angle in five-axis surface machining with torus cutter-s.The International Journal of Advanced Manufacturing Technology, vol.107, no. 4, p. 4261-4271, DOI:10.1007/s00170-020-052714.

London Journal Press Membership

For Authors, subscribers, Boards and organizations

London Journals Press membership is an elite community of scholars, researchers, scientists, professionals and institutions associated with all the major disciplines. London Journals Press memberships are for individuals, research institutions, and universities. Authors, subscribers, Editorial Board members, Advisory Board members, and organizations are all part of member network.

Read more and apply for membership here:
https://journalspress.com/journals/membership

For Authors

Author Membership provide access to scientific innovation, next generation tools, access to conferences/seminars /symposiums/webinars, networking opportunities, and privileged benefits.
Authors may submit research manuscript or paper without being an existing member of LJP. Once a non-member author submits a research paper he/she becomes a part of "Provisional Author Membership".

For Institutions

Society flourish when two institutions come together." Organizations, research institutes, and universities can join LJP Subscription membership or privileged "Fellow Membership" membership facilitating researchers to publish their work with us, become peer reviewers and join us on Advisory Board.

For Subscribers

Subscribe to distinguished STM (scientific, technical, and medical) publisher. Subscription membership is available for individuals universities and institutions (print & online). Subscribers can access journals from our libraries, published in different formats like Printed Hardcopy, Interactive PDFs, EPUBs, eBooks, indexable documents and the author managed dynamic live web page articles, LaTeX, PDFs etc.

GO GREEN AND HELP
SAVE THE ENVIRONMENT

JOURNAL AVAILABLE IN

PRINTED VERSION, INTERACTIVE PDFS, EPUBS, EBOOKS, INDEXABLE DOCUMENTS AND THE AUTHOR MANAGED DYNAMIC LIVE WEB PAGE ARTICLES, LATEX, PDFS, RESTRUCTURED TEXT, TEXTILE, HTML, DOCBOOK, MEDIAWIKI MARKUP, TWIKI MARKUP, OPML, EMACS ORG-MODE & OTHER

SCAN TO KNOW MORE

support@journalspress.com
www.journalspress.com

*THIS JOURNAL SUPPORT AUGMENTED REALITY APPS AND SOFTWARES